NFATC2IP is a mediator of SUMO-dependent genome integrity

Tiffany Cho,[1,2] Lisa Hoeg,[1] Dheva Setiaputra,[1,3] and Daniel Durocher[1,2]

[1]Lunenfeld-Tanenbaum Research Institute, Mount Sinai Hospital, Toronto, Ontario M5G 1X5, Canada; [2]Department of Molecular Genetics, University of Toronto, Toronto, Ontario M5S 1A8, Canada; [3]Department of Molecular Biology and Biochemistry, Simon Fraser University, Burnaby, British Columbia V5A 1S6, Canada

The post-translational modification of proteins by SUMO is crucial for cellular viability and mammalian development in part due to the contribution of SUMOylation to genome duplication and repair. To investigate the mechanisms underpinning the essential function of SUMO, we undertook a genome-scale CRISPR/Cas9 screen probing the response to SUMOylation inhibition. This effort identified 130 genes whose disruption reduces or enhances the toxicity of TAK-981, a clinical-stage inhibitor of the SUMO E1-activating enzyme. Among the strongest hits, we validated and characterized NFATC2IP, an evolutionarily conserved protein related to the fungal Esc2 and Rad60 proteins that harbors tandem SUMO-like domains. Cells lacking NFATC2IP are viable but are hypersensitive to SUMO E1 inhibition, likely due to the accumulation of mitotic chromosome bridges and micronuclei. NFATC2IP primarily acts in interphase and associates with nascent DNA, suggesting a role in the postreplicative resolution of replication or recombination intermediates. Mechanistically, NFATC2IP interacts with the SMC5/6 complex and UBC9, the SUMO E2, via its first and second SUMO-like domains, respectively. AlphaFold-Multimer modeling suggests that NFATC2IP positions and activates the UBC9–NSMCE2 complex, the SUMO E3 ligase associated with SMC5/SMC6. We conclude that NFATC2IP is a key mediator of SUMO-dependent genomic integrity that collaborates with the SMC5/6 complex.

The covalent attachment of the SUMO polypeptide on substrate proteins controls multiple nuclear processes that include gene expression, RNA processing, protein stability, and genome integrity (Jackson and Durocher 2013; Vertegaal 2022). The human genome encodes three SUMO isoforms that are conjugated onto proteins: SUMO1 and the nearly identical SUMO2/3 proteins. SUMO conjugation requires a multienzymatic cascade that is initiated by an E1-activating enzyme (formed by SAE1–UBA2) that uses ATP to activate SUMO and transfer it to a single E2-conjugating enzyme, UBC9 (also known as UBE2I). The resulting high-energy UBC9~SUMO thioester intermediate poises SUMO for transfer, usually by creation of an isopeptide bond with the ε-amino group of a lysine residue on the target protein often located within the consensus sequence ΨKxE, where Ψ is a large hydrophobic residue, and x represents any residue. While SUMOylation has been detected on thousands of proteins (Hendriks and Vertegaal 2016), the human genome encodes only eight SUMO E3 ligases: the PIAS1–4 proteins,

the SMC5/6-associated protein NSMCE2, RANBP2, and the SMIZ1/2 proteins (Vertegaal 2022). Only SUMO2/3 can form poly-SUMO chains via their Lys11 residues, whereas SUMO1 is used for mono-SUMO and multi-SUMO modifications or to cap SUMO chains.

SUMOylation is an essential process for both embryonic development and cellular proliferation, as demonstrated by the early embryonic lethality of the *Ubc9* knockout in mice and the pan-essentiality of *UBC9* in hundreds of cancer cell lines screened in the dependency map (DepMap) (Nacerddine et al. 2005; Dempster et al. 2019). The *Ubc9* knockout mice die with massive chromosome instability, identifying genome maintenance as a key function for SUMOylation (Nacerddine et al. 2005). Interestingly, out of the eight known SUMO E3 ligases, only RANBP2 and NSMCE2 are encoded by essential genes in human cells as per DepMap, and of those, only NSMCE2 is clearly associated with chromosome stability as part of its role within the SMC5/6 complex (Peng and Zhao 2023). The SUMO E3 ligase activity of the SMC5/6 complex is involved in promoting DNA

replication and DNA repair by homologous recombination, and genetic loss of SMC5/6 complex members compromises cell viability with phenotypes consistent with chromosomal instability, including highly penetrant chromosome bridging (Gallego-Paez et al. 2014; Payne et al. 2014; Jacome et al. 2015; Pryzhkova and Jordan 2016; Peng and Zhao 2023).

In addition to the involvement of SUMO in SMC5/6-dependent genome stability, SUMO plays a central role in a number of additional genome maintenance pathways. For example, SUMO1 modification of the base excision repair enzyme TDG promotes its release from abasic sites, thereby promoting completion of the repair reaction (Hardeland et al. 2002; Baba et al. 2005). In another example, in human cells, SUMO and the SUMO modification machinery localize to DNA double-strand breaks (DSBs), where they help orchestrate recruitment of proteins to DSB sites (Galanty et al. 2009; Morris et al. 2009). Furthermore, investigation of the role of SUMO during DNA repair by homologous recombination led to the concept that SUMO acts via group modification of target proteins, where multiple components of a pathway are SUMOylated to strengthen their collective action (Psakhye and Jentsch 2012; Vertegaal 2022). Group modification regulates biological processes in large part by nucleating protein–protein interactions, and to this end, SUMO-modified proteins can be recognized by SUMO-interacting motifs (SIMs). In one example, cross-talk between SUMO and the ubiquitin machinery exists through the action of SUMO targeted ubiquitin ligases (STUbls), which are E3 ubiquitin ligases that recognize SUMOylated substrates to regulate their proteolysis. The prototypical STUbl is the evolutionarily conserved RNF4 protein, which recognizes poly-SUMOylated proteins via tandem SIM motifs (Xu et al. 2014) to regulate genome stability (Prudden et al. 2007).

The central role of SUMOylation in numerous cellular processes relevant to cancer motivated the development of small molecule inhibitors of SUMOylation by targeting the single SUMO E1 enzyme formed by SAE1–UBA2 and led to the discovery of TAK-981 (Langston et al. 2021), which is currently being investigated in clinical trials in combination with pembrolizumab, a cancer immunotherapy (trial NCT04381650). This trial was spurred by the observation that SUMO suppresses type I interferon (IFN1) responses, which is central to antitumor immunity (Lightcap et al. 2021). However, it is likely that pharmacological modulation of SUMOylation will have additional cell-intrinsic therapeutic benefits.

In this work, we sought to identify key mediators of SUMO-dependent genome integrity. To do so, we undertook a genome-scale CRISPR/Cas9 screen to identify genes that contribute to the cellular resistance to inhibition of the SUMO E1 enzyme. Apart from the gene encoding the MRP1 multidrug transporter, by far the top hit in this screen was the gene encoding the NFATC2IP protein (also known as NIP45), a protein with tandem SUMO-like domains that is the likely ortholog of the fungal Esc2/Rad60 proteins (Novatchkova et al. 2005). We report that NFATC2IP promotes SUMO-dependent genome maintenance via a functional interaction with the SMC5/6 complex and propose a model in which NFAT-C2IP activates the NSMCE2 SUMO E3 ligase by simultaneously interacting with UBC9 and SMC5.

Results

A chemogenetic map of SUMOylation inhibition

In a recent chemogenetic survey of the response to genotoxic agents undertaken by our group (Olivieri et al. 2020), we screened for genes that modulate sensitivity to MLN4924, an inhibitor of the NEDD8 E1, since this agent is known to cause DNA damage (Soucy et al. 2009). The rich set of genetic interactions uncovered in the MLN4924 screen motivated us to chart the genetic architecture of the response to SUMOylation inhibition caused by treatment with the SAE1–UBA2 complex (SUMO E1) inhibitor TAK-981 (Langston et al. 2021). The screen was carried out in hTERT immortalized retinal pigment epithelial-1 (RPE1-hTERT) $TP53^{-/-}$ cells stably expressing Cas9 (Zimmermann et al. 2018) at a dose that killed ~20% of cells (LD$_{20}$), as depicted in Supplemental Figure S1A and as described previously (Olivieri et al. 2020; Olivieri and Durocher 2021). Gene-level normalized Z-scores (normZ) were computed using DrugZ (Colic et al. 2019) and are shown in Figure 1A and Supplemental Table S1. To remain consistent with the analyses of Olivieri et al. (2020), we selected normZ values less than −3 with false discovery rates (FDRs) <15% to identify genes whose mutation caused sensitization to the inhibitors. No single gene had a normZ value >6, which we previously set as the threshold for genes that are causing resistance to drug treatment (Olivieri et al. 2020). These cutoffs identified a total of 130 genes whose disruption caused sensitivity to TAK-981 (Fig. 1A; Supplemental Table S1). We analyzed the connectivity of the 130 genes by building networks based on protein–protein interactions using STRING (Supplemental Fig. S1B; Supplemental Table S2; Szklarczyk et al. 2021) or gene–gene essentiality score correlations in DepMap (Supplemental Fig. S2; Supplemental Table S2; Dempster et al. 2019). These analyses revealed that the TAK-981 screen identified physically, genetically, and functionally interconnected sets of genes. In a similar vein, functional term analysis using ShinyGO (Ge et al. 2020) for enrichment in the gene ontology (GO) terms biological process, molecular function, or cellular compartment showed enrichments that were consistent with SUMO biology such as cellular response to DNA damage stimulus (GO:0006974; 7.4×10^{-5} genes), DNA-binding transcription factor binding (GO:0003700; 1.8×10^{-5} genes), and nuclear protein-containing complex (GO:0140513; 2.2×10^{-4} genes), respectively (Supplemental Fig. S3A–C). From these analyses, we conclude that the TAK-981 screen was successful in probing pathways that are relevant to SUMOylation, and this motivated a search for factors that may mediate the role of SUMO in genomic integrity.

The top-scoring gene in the TAK-981 screen was *ABCC1*, encoding MRP1 (Robey et al. 2018), suggesting
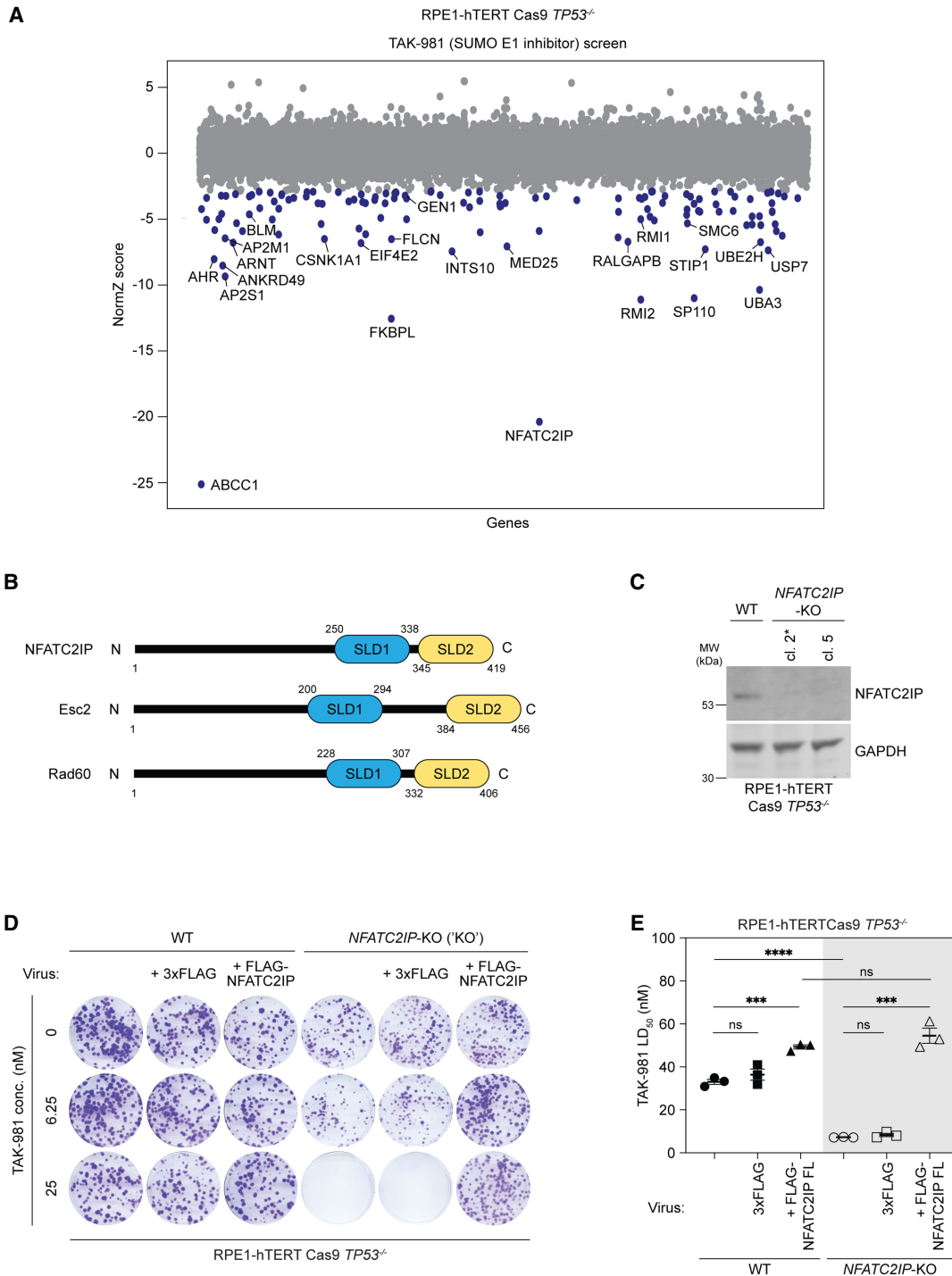
A

B

C

D

E

Figure 1. NFATC2IP promotes viability in response to SUMOylation inhibition. (*A*) Chemogenomic CRISPR screen result for RPE1-hTERT Cas9 *TP53*$^{-/-}$ cells treated with the SUMO E1 inhibitor TAK-981. Each data point represents a gene score (normZ value) for an individual gene, calculated using DrugZ. Blue points represent sensitizing genes (normZ < −3 with FDR < 0.15). (*B*) Schematic of the structural domains of the human NFATC2IP protein and its fungal orthologs, Esc2 and Rad60. (SLD1) SUMO-like domain 1, (SLD2) SUMO-like domain 2. (*C*) Immunoblot analyses of clonal *NFATC2IP*-KO cell lines produced by gene editing (Supplemental Table S4). GAPDH was used as a loading control. The asterisk (*) indicates the *NFATC2IP*-KO clone that was used for all further experiments in this study. (*D,E*) Survival of TAK-981 treatment determined by clonogenic survival assays in parental RPE1-hTERT Cas9 *TP53*$^{-/-}$ (WT) or isogenic *NFATC2IP*-KO cells that either were left untransduced or were transduced with lentivirus expressing FLAG-tagged NFATC2IP or 3×FLAG alone. Representative images of the clonogenic survival assays are shown in *D*, and quantitation is shown in *E*. Data are shown as the mean TAK-981 LD$_{50}$ ± SEM. (*n* = 3). Statistical comparisons were performed using two-tailed unpaired *t*-tests. (****) *P* < 0.0001, (***) *P* < 0.001, (ns) *P* ≥ 0.05. (FL) Full-length.

that TAK-981 is a substrate of this multidrug transporter. The next top hits were *NFATC2IP*, which is discussed at length below; *FKBPL*, which encodes a poorly characterized protein that interacts with ANKRD49, encoded by another hit in this screen (Taipale et al. 2014; Hart et al. 2015); *RMI2*, coding for a member of the BLM–TOPIIIα–RMI1/2 (BTRR) complex involved in multiple DNA transactions (Bythell-Douglas and Deans 2021), with the genes encoding BLM and RMI1 also present among the top 50 hits; and *SP110*, encoding a "speckle protein" family member that localizes to promyelocytic (PML) bodies, sites of high SUMO activity (Fraschilla and Jeffrey 2020). As most of these proteins were previously only loosely linked to SUMO, this screen highlights their importance in supporting the viability of human cells to perturbation of SUMOylation.

NFATC2IP promotes survival in response to SUMOylation inhibition

NFATC2IP (also known as *NIP45*) attracted our interest because it encodes a protein featuring two SUMO-like domains (SLDs) (Fig. 1B) and is the likely ortholog of the *Saccharomyces cerevisiae* Esc2 and *Schizosaccaromyces pombe* Rad60 proteins (Fig. 1B; Novatchkova et al. 2005). In yeast species, Esc2 and Rad60 promote replication fork integrity and tolerance of replication stress (Morishita et al. 2002; Boddy et al. 2003; Miyabe et al. 2006), but surprisingly, in human cells, NFATC2IP had only been described as a cofactor of the nuclear factor of activated T cells, cytoplasmic 2 (NFATc2) transcription factor (Hodge et al. 1996). Since NFATc2 was not a hit in the TAK-981 screen (Supplemental Table S1) and since the TAK-981 screen hits were instead enriched for genes acting in the response to DNA damage (such as *BLM* and *RMI1/2*) (Fig. 1A; Supplemental Fig. S3A), we asked whether NFATC2IP promoted the normal cellular resistance to SUMOylation inhibition through a role in genome maintenance.

We generated clonal knockouts (KOs) of *NFATC2IP* in RPE1-hTERT $TP53^{-/-}$ Cas9 cells (Fig. 1C; Supplemental Fig. S4A,B) with CRISPR gene editing that produced a biallelic 1-nt deletion (c.493delC) causing a frameshift mutation (p.His165MetfsX15). Using these clonal *NFATC2IP*-KO cells, we assessed the half-maximal lethal dose (LD$_{50}$) of TAK-981 in clonogenic survival assays. Loss of NFATC2IP decreased the TAK-981 LD$_{50}$ from 28.5 nM ± 2.5 nM in the parental cell line to 7.0 nM ± 0.8 nM (Fig. 1D,E; Supplemental Fig. S4C,D). This hypersensitivity of *NFATC2IP*-KO cells was fully reversed by reintroducing exogenous NFATC2IP expressed as 3xFLAG-tagged protein from a lentiviral vector (WT) (Fig. 1D,E; Supplemental Fig. S4C,D). We conclude that NFATC2IP promotes cell survival upon SUMOylation inhibition.

NFATC2IP promotes genomic integrity

Given the role of NFATC2IP orthologs in genome maintenance, as well as the central role of SUMO in protecting genome integrity, we tested whether loss of NFATC2IP caused genome instability. We monitored micronuclea-

tion, a sensitive readout of genome instability (Fenech et al. 2011), in parental and *NFATC2IP*-KO cells with or without TAK-981 treatment using an automated microscopy pipeline. When SUMOylation is unperturbed, loss of NFATC2IP did not impact micronucleation levels (Fig. 2A,B). However, following SUMO E1 inhibition, *NFATC2IP*-KO cells displayed enhanced micronucleus (MN) formation at all doses, and this phenotype was entirely suppressed by re-expression of NFATC2IP tagged with either 3xFLAG or GFP (Fig. 2A,B; Supplemental Fig. S5A–C). NFATC2IP therefore suppresses the genome instability caused by inhibition of SUMOylation.

MN formation can occur via two broadly distinct routes: either through whole-chromosome missegregation or through the segregation of acentric fragments (Fenech et al. 2011). It is possible to distinguish between these possibilities simply by monitoring kinetochores and centromeres using anticentromere antibodies (ACA). We observed that upon TAK-981 treatment, it is specifically centromere-negative (ACA⁻) MNs that are increased in *NFATC2IP*-KO cells compared with wild-type cells (Fig. 2B). These results suggest that NFATC2IP guards against acentric chromosome missegregation when SUMOylation is impaired. However, these acentric fragments are unlikely to be caused by chromosomal breaks occurring in interphase, since we observed that while micronucleation was starting to be observed after 48 h of TAK-981 treatment, we did not detect an overt increase in γ-H2AX levels in *NFATC2IP*-KO cells until 72 h of SUMO E1 inhibition (Supplemental Fig. S6A,B). We also did not detect a more pronounced impact of TAK-981 treatment on the cell cycle distribution of *NFATC2IP*-KO cells treated with the SUMO E1 inhibitor compared with the parental counterparts (Supplemental Fig. S6C–E); however, we did detect a DNA synthesis defect in *NFATC2IP*-KO cells treated with TAK-981 (Supplemental Fig. S6C,F), which is discussed further below.

We also observed that the combined loss of NFATC2IP and TAK-981 treatment was accompanied by the formation of long chromatin bridges connecting two nuclei (Fig. 2C). We quantitated the formation of DAPI-stained chromatin bridges and binned the data according to whether we observed cells with normal chromatin or those that displayed either short (<15-µm) or long (>15-µm) chromatin bridges. We observed that loss of NFATC2IP led to an increase in long chromatin bridges following TAK-981 treatment at all doses tested compared with the parental cell line, with the strongest effect seen at the 50 nM TAK-981 dose (Fig. 2D). As with micronucleation, SUMOylation inhibition on its own is able to induce chromatin bridge formation, but *NFATC2IP*-KO cells accumulate bridges at higher frequency and at lower concentrations of TAK-981 than wild-type cells, indicating that the loss of NFATC2IP exacerbates a pathological process induced by inhibition of the SUMO E1 (Fig. 2D). Since breakage of chromatin bridges during cytokinesis can generate acentric fragments (Warecki and Sullivan 2020; Hong et al. 2021), we surmise that they are a source for the observed micronucleation and, possibly, the hypersensitivity of *NFATC2IP*-KO cells to SUMO E1 inhibition.
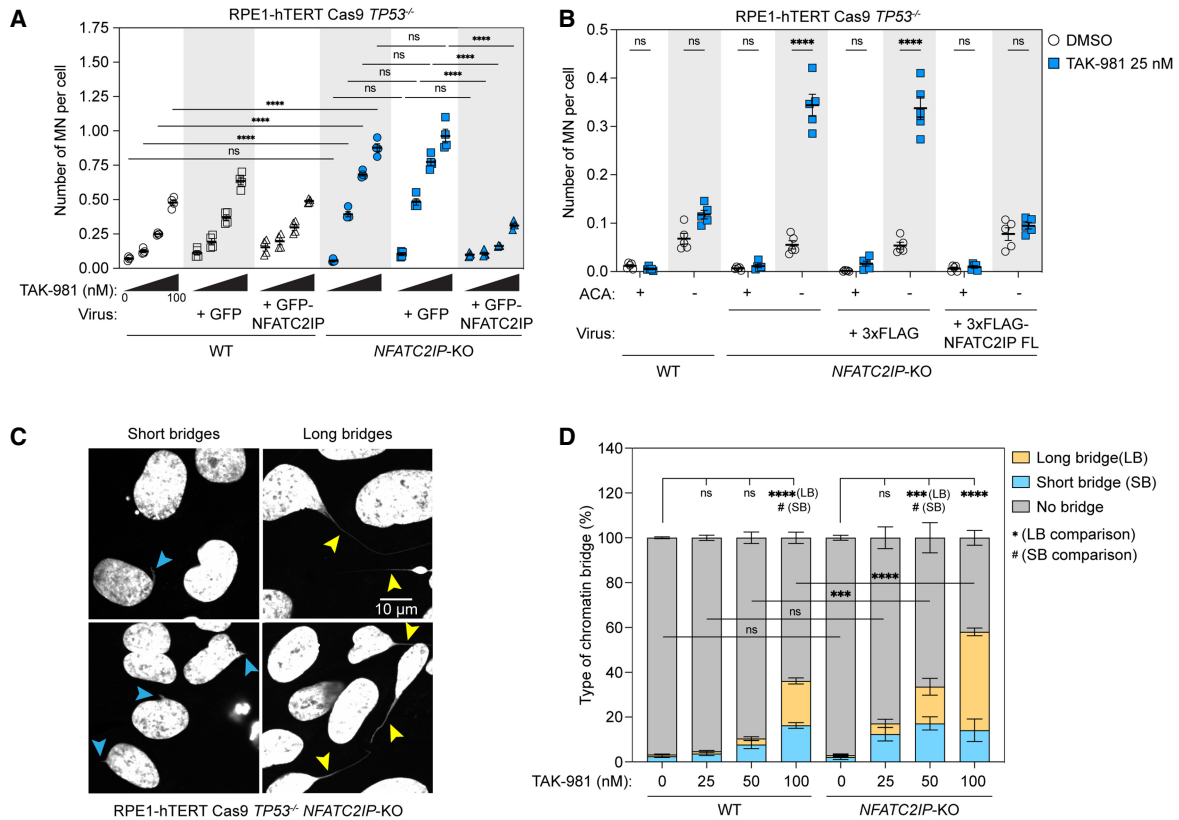
Figure 2. *NFATC2IP* promotes genome integrity in response to SUMOylation inhibition. (*A*) Quantitation of MN formation after treatment with increasing doses of TAK-981 for 72 h in RPE-hTERT Cas9 *TP53*$^{-/-}$ (WT) or *NFATC2IP*-KO cells that either were left untransduced or were transduced with the indicated lentivirus. A minimum of 455 nuclei was counted for each condition. Bars represent the mean ± SEM. (*n* = 4). Multiple unpaired *t*-tests were used for statistical analyses with Bonferroni–Dunn correction. (****) $P < 0.0001$, (ns) $P \geq 0.05$. (*B*) Quantitation of ACA-positive or ACA-negative MN formation after treatment with or without 25 nM TAK-981 for 48 h in parental RPE1-hTERT Cas9 *TP53*$^{-/-}$ (WT) or isogenic *NFATC2IP*-KO cells that either were left untransduced or were transduced with the indicated lentivirus. A minimum of 273 nuclei was counted for each condition. Bars represent the mean ± SEM. (*n* = 5). (FL) Full-length. Multiple unpaired *t*-tests were used for analyses with Bonferroni–Dunn correction. (****) $P < 0.0001$, (ns) $P \geq 0.05$. (*C*) Representative micrographs of chromatin bridge formation visualized by DAPI staining. Blue arrowheads point to chromatin bridges that were identified as short bridges (less than ~15 μm), and yellow arrowheads point to long chromatin bridges (more than ~15 μm). Scale bar, 10 μm. (*D*) Quantitation of nuclei displaying chromatin bridges following treatment with the indicated doses of TAK-981 for 24 h in RPE1-hTERT Cas9 *TP53*$^{-/-}$ (WT) or isogenic *NFATC2IP*-KO cells. A minimum of 263 nuclei was assessed for each condition. Bars represent the mean ± SEM. (*n* = 3). Analyses were performed using two-way ANOVA with Tukey's multiple comparison testing. For comparisons of long chromatin bridges, (****) $P < 0.0001$, (***) $P < 0.001$, (ns) $P \geq 0.05$. For comparisons of short chromatin bridges, only significant comparisons are shown. (#) $P < 0.05$. (LB) Long bridge, (SB) short bridge.

NFATC2IP acts in interphase to promote genome maintenance

Chromatin bridges can originate either from defective DNA replication, repair, or recombination or via the failure to complete mitotic processes such as chromosome decatenation (Hong et al. 2021). To begin distinguishing between these possibilities, we asked whether NFATC2IP acted to promote genome integrity in interphase or during mitosis. To do so, we fused a nuclear export signal (NES) to NFATC2IP so that it could only access chromatin after nuclear envelope breakdown at the onset of mitosis. NES-based export is a common mechanism to temporally restrict access of proteins to mitotic chromatin, with GEN1 and CIP2A being two clear examples of mitotic genome maintenance factors controlled in that fashion

(Chan and West 2014; De Marco Zompit et al. 2022). We also fused a mutant form of the NES (NESm) that substitutes the two last leucine residues of the canonical LxxxLxxLxL NES consensus sequence to alanine as a means to control for the potential impact of the NES fusion itself (Fig. 3A). As expected, the NES-NFATC2IP proteins, expressed either as GFP or 3xFLAG fusions, were restricted to the cytoplasm during interphase, whereas NESm-NFATC2IP resided in the nucleus (Supplemental Fig. S7A–C). While NESm-NFATC2IP expression fully restored the viability of *NFATC2IP*-KO cells to SUMOylation inhibition, NES-NFATC2IP only partially restored resistance (Fig. 3B,C; Supplemental Fig. S7D–G). Similar results were also obtained by examining micronucleation: NESm-NFATC2IP completely rescued the high micronucleation levels of *NFATC2IP*-KO cells treated with TAK-
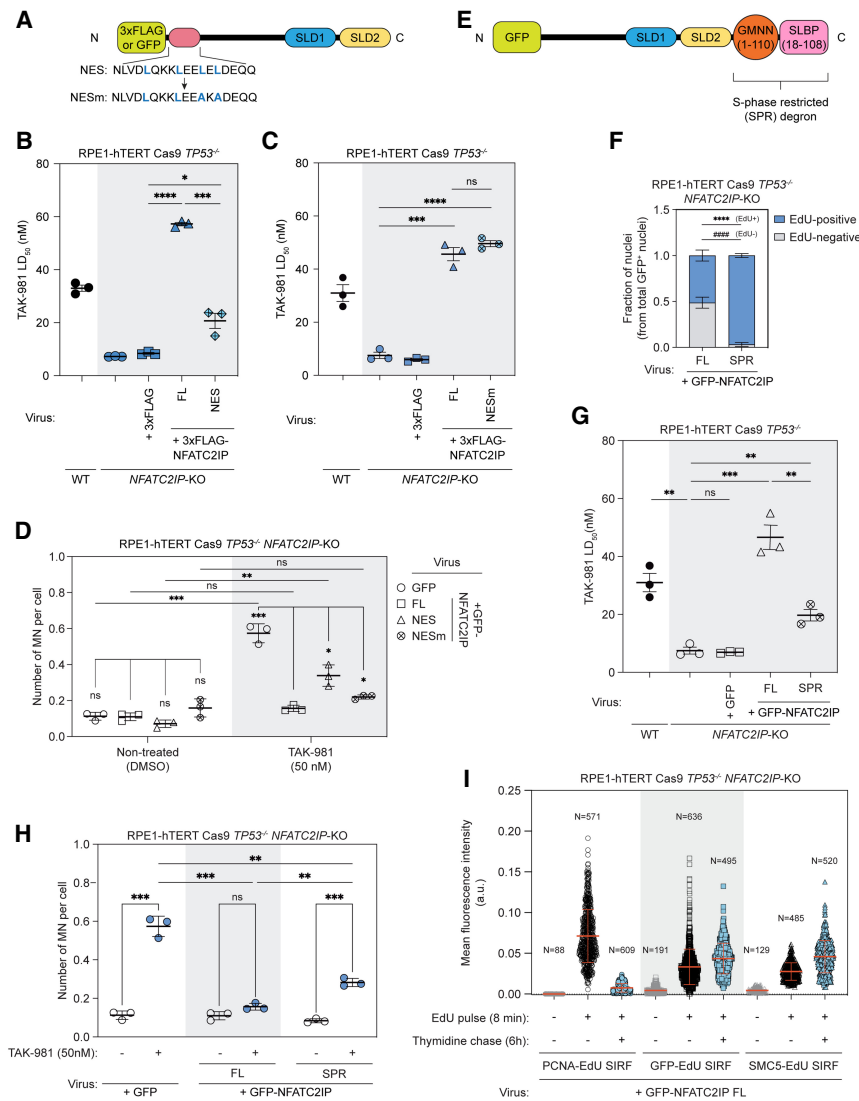
Figure 3. NFATC2IP functions in interphase. (*A*) Schematic of the epitope-tagged NFATC2IP proteins fused to a nuclear export signal (NES) or a mutant form of the NES (NESm). (SLD1) SUMO-like domain 1, (SLD2) SUMO-like domain 2. (*B,C*) Determination of TAK-981 LD$_{50}$ values from dose response clonogenic survival assays in parental RPE1-hTERT Cas9 $TP53^{-/-}$ (WT) or isogenic *NFATC2IP*-KO cells that either were left untransduced or were transduced with a lentivirus encoding the indicated protein. (*B*) Quantitation of TAK-981 LD$_{50}$ in cells expressing NES-fused NFATC2IP protein. Data are shown as the mean ± SEM. (*n* = 3). (FL) Full-length, (NES) NES-NFATC2IP. Statistical analyses were performed with two-tailed unpaired *t*-tests. (****) $P < 0.0001$, (***) $P < 0.001$, (*) $P < 0.05$. (*C*) Quantitation of TAK-981 LD$_{50}$ in cells expressing NFATC2IP protein fused with the mutant form of NES. Data are shown as the mean ± SEM. (*n* = 3). (FL) Full-length NFATC2IP, (NESm) NESm-NFATC2IP. Statistical analyses were performed with two-tailed unpaired *t*-tests. (****) $P < 0.0001$, (***) $P < 0.001$, (ns) $P \geq 0.05$. (*D*) Quantitation of MN formation after treatment with 50 nM TAK-981 for 48 h. RPE1-hTERT Cas9 $TP53^{-/-}$ *NFATC2IP*-KO cells were transduced with lentivirus encoding the indicated protein. Data are shown as the number of MNs per cell, and a minimum of 495 nuclei was counted for each condition. Bars represent the mean ± SD. (*n* = 3). (FL) Full-length NFATC2IP, (NES) NES-NFATC2IP, (NESm) NESm-NFATC2IP. Data were analyzed by performing multiple unpaired *t*-tests with Bonferroni–Dunn correction. (***) $P < 0.001$, (**) $P < 0.01$, (*) $P < 0.05$, (ns) $P \geq 0.05$. (*E*) Schematic of the GFP-NFATC2IP protein fused to an S-phase-restricted (SPR) degron consisting of protein fragments of geminin (GMNN) and stem–loop binding protein (SLBP). (SLD1) SUMO-like domain 1, (SLD2) SUMO-like domain 2. (*F*) Quantitation of GFP-positive nuclei displaying EdU (5-ethynyl-2′-deoxyuridine) incorporation in RPE1-hTERT Cas9 $TP53^{-/-}$ *NFATC2IP*-KO cells that were transduced with lentivirus encoding the indicated protein. A minimum of 104 GFP-positive nuclei was analyzed per replicate to assess EdU incorporation. Bars represent the mean ± SD. (*n* = 4). (FL) Full-length NFATC2IP, (SPR) NFATC2IP-SPR. Two-way ANOVA testing was performed for statistical comparisons. For comparison of EdU⁺ GFP⁺ nuclei, (****) $P < 0.0001$. For comparison of EdU⁻ GFP⁺ nuclei, (####) $P < 0.0001$. (*G*) Determination of TAK-981 LD$_{50}$ values from dose response clonogenic survival assays in parental RPE1-hTERT Cas9 $TP53^{-/-}$ (WT) or isogenic *NFATC2IP*-KO cells that either were left untransduced or were transduced with a lentivirus encoding the indicated protein. Data are shown as the mean ± SEM. (*n* = 3). (FL) Full-length NFATC2IP, (SPR) NFATC2IP-SPR. For statistical analyses, two-tailed unpaired *t*-tests were performed. (***) $P < 0.001$, (**) $P < 0.01$, (ns) $P \geq 0.05$. (*H*) Quantitation of MN formation after treatment with 50 nM TAK-981 for 48 h. RPE1-hTERT Cas9 $TP53^{-/-}$ *NFATC2IP*-KO cells were transduced with a lentivirus encoding the indicated protein. A minimum of 495 nuclei was counted per replicate. Bars represent the mean ± SD. (*n* = 3). (FL) Full-length NFATC2IP, (SPR) NFATC2IP-SPR. Data were analyzed using multiple unpaired *t*-tests with Bonferroni–Dunn correction. (***) $P < 0.001$, (**) $P < 0.01$, (ns) $P \geq 0.05$. (*I*) Quantitation of proximity ligation signal with biotin-conjugated EdU (SIRF) in RPE1-hTERT Cas9 $TP53^{-/-}$ *NFATC2IP*-KO cells transduced with a lentivirus encoding GFP-NFATC2IP. EdU was pulsed for 8 min at a concentration of 125 µM, and DMSO was added in the no-EdU control. For the thymidine chase condition, a portion of the EdU-pulsed cells was incubated in thymidine-containing media (100 µM) for 6 h. For the conditions that included an EdU pulse, data are shown as mean fluorescence intensity (MFI) of the proximity ligation signal generated between biotin-conjugated EdU and the indicated protein in nuclei displaying Alexa fluor 647/EdU costaining. For the negative control, all DAPI-stained nuclei were analyzed to calculate the proximity ligation MFI values. Bars represent the mean ± SD of MFI data combined from repeated independent experiments (for negative control and EdU pulse-only conditions, *n* = 3; for EdU pulse + thymidine chase condition, *n* = 2). Numbers of combined data points in each condition are indicated. (FL) Full-length NFATC2IP, (a.u.) arbitrary units.
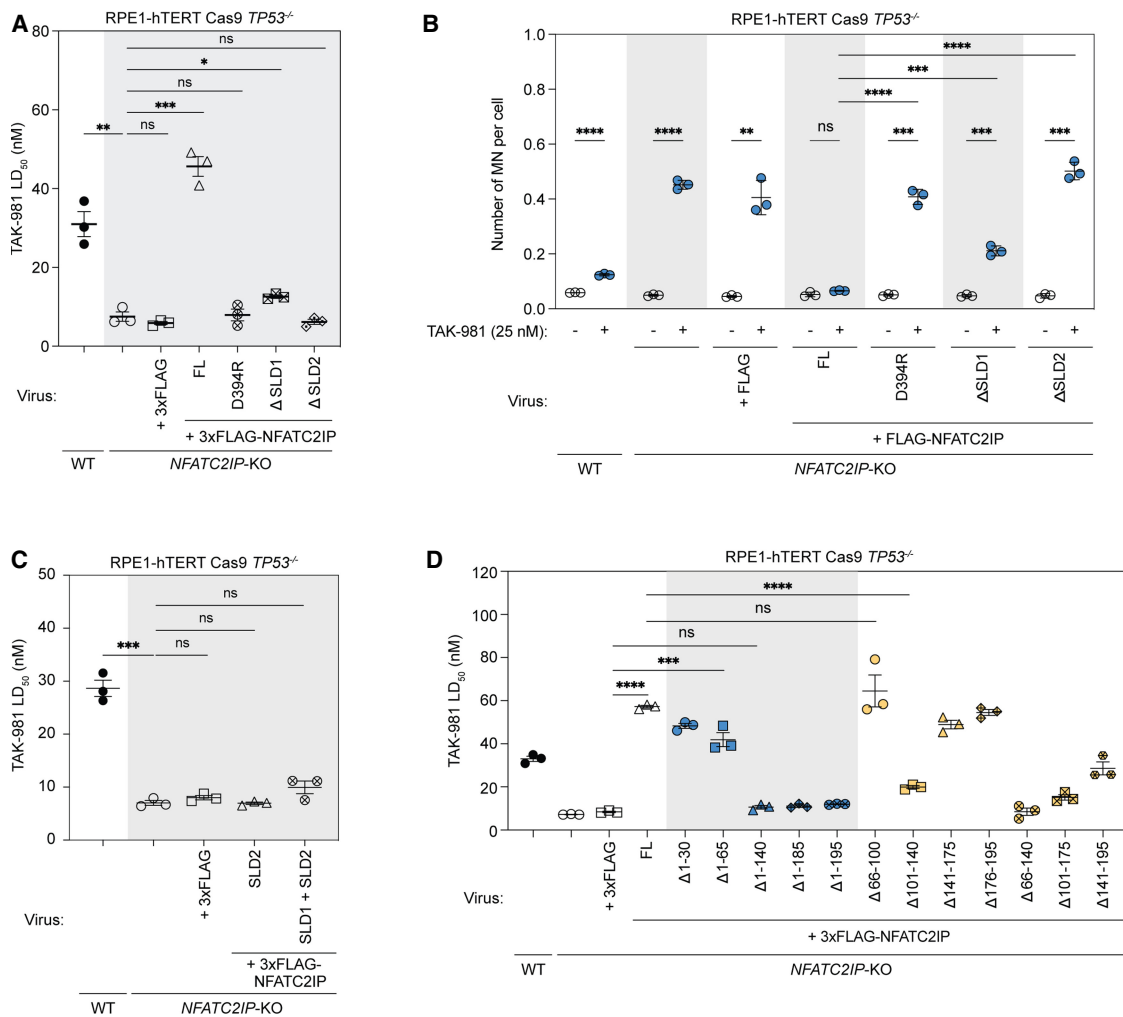
Figure 4. Structure–function analysis of NFATC2IP. (*A–D*) RPE1-hTERT Cas9 *TP53*$^{-/-}$ (WT) or isogenic *NFATC2IP*-KO cells either were left untransduced or were transduced with lentivirus encoding the indicated protein. (FL) Full-length. (*A*) Determination of TAK-981 LD$_{50}$. Data are shown as the mean ± SEM. (*n* = 3). Statistical comparisons were performed with two-tailed unpaired *t*-tests. (***) *P* < 0.001, (**) *P* < 0.01, (*) *P* < 0.05, (ns) *P* ≥ 0.05. (ΔSLD1) Deletion of residues 256–344, (ΔSLD2) deletion of residues 345–419. (*B*) Quantitation of MN formation after treatment with 25 nM TAK-981 for 48 h. Data are shown as the number of MNs per cell, and a minimum of 1229 nuclei per replicate were counted for each condition. Bars represent the mean ± SD. (*n* = 3). Data were analyzed with multiple unpaired *t*-tests with Bonferroni–Dunn correction. (****) *P* < 0.0001, (***) *P* < 0.001, (**) *P* < 0.01, (ns) *P* ≥ 0.05. (ΔSLD1) Deletion of residues 256–344, (ΔSLD2) deletion of residues 345–419. (*C*) Determination of TAK-981 LD$_{50}$. Data are shown as the mean ± SEM (*n* = 3) and were analyzed with two-tailed unpaired *t*-tests. (***) *P* < 0.001, (ns) *P* ≥ 0.05. (SLD2) NFATC2IP amino acid residues 345–419, (SLD1+2) NFATC2IP amino acid residues 251–419. (*D*) Determination of TAK-981 LD$_{50}$. Data are shown as the mean ± SEM (*n* = 3) and were analyzed with two-tailed unpaired *t*-tests. (****) *P* < 0.0001, (***) *P* < 0.001, (ns) *P* ≥ 0.05. Deletion mutants of NFATC2IP are schematized in Supplemental Figure S11.

981, whereas NES-NFATC2IP only partially did so (Fig. 3D). These observations are consistent with NFATC2IP acting mainly during interphase and requiring access to chromatin prior to mitosis to promote genome integrity when SUMOylation is impaired. However, the residual activity of NES-NFATC2IP suggests that NFATC2IP may also be required during mitosis.

To further probe this possibility, we developed an NFATC2IP protein with expression tightly restricted to S phase by fusing NFATC2IP to a composite degron named SPR (S-phase-restricted), formed by adjoining fragments of the geminin (GMNN) and SLBP proteins (A Duringer, P Anterieux, A Loiselle, C Goupil, and Y Doyon, in prep.) (Fig. 3E).

Analysis of lentivirally mediated NFATC2IP-SPR expression in *NFATC2IP*-KO cells confirmed that the NFATC2IP-SPR protein could only be detected in cells actively replicating DNA, since 97% of the cells expressing NFATC2IP were also positive for EdU (5-ethynyl-2′-deoxyuridine) incorporation (Fig. 3F; Supplemental Fig. S8A,B). Similarly, monitoring of NFATC2IP-SPR expression by immunoblotting showed that it peaked in concert with DNA replication, ~4 h prior to that of cyclin A, whose expression culminates prior to mitotic entry (Supplemental Fig. S8C–F). Interestingly, the S-phase-restricted NFATC2IP-SPR protein partially rescued both the hypersensitivity and increased micronucleation of *NFATC2IP*-KO cells

in response to SUMOylation inhibition (Fig. 3G,H; Supplemental Fig. S8G). These results suggest that NFATC2IP acts during S phase, which is also supported by the EdU incorporation defect observed in *NFATC2IP*-KO cells (Supplemental Fig. S6F). Furthermore, it is clear that NFATC2IP activity is additionally required outside of S phase to promote cell survival and genome stability under conditions of limiting SUMOylation.

Consistent with a possible role for NFATC2IP in S phase, NFATC2IP was identified as localizing to nascent DNA by iPOND-MS (Wessel et al. 2019). This suggested that NFATC2IP may function during replication or postreplicatively. In support of this possibility, NFATC2IP-GFP could be found in proximity to nascent DNA as measured by proximity ligation assays with EdU, also known as SIRF (Fig. 3I; Supplemental Fig. S9A–D; Roy et al. 2018; Roy and Schlacher 2019). We monitored PCNA localization to nascent DNA at positive control and included SMC5 in these studies, for reasons that are elaborated below. Whereas the proximity ligation signal between PCNA and EdU was abrogated following a thymidine chase, indicating that PCNA is located at sites of DNA synthesis, we observed that NFATC2IP and SMC5 remained in proximity to newly synthesized DNA even after a thymidine chase (Fig. 3I; Supplemental Fig. S9A–D), consistent with a postreplicative function.

Structure–function analysis of NFATC2IP

To gain insights into the mechanism by which NFATC2IP may promote genomic integrity when SUMOylation is inhibited, we assessed the involvement of SLD1 and SLD2 (Fig. 1B) in promoting cell survival in response to TAK-981 treatment. We expressed, in *NFATC2IP*-KO cells, NFATC2IP lacking either SLD1 (ΔSLD1) or SLD2 (ΔSLD2) or a variant that harbored the D394R mutation in SLD2 that corresponds to Rad60 E380R, a point mutation that abolishes the interaction of SLD2 with the SUMO E2 UBC9 (Prudden et al. 2009, 2011; Sekiyama et al. 2010). We found that loss of either SLD failed to restore normal resistance to TAK-981, with the phenotype being more pronounced with ΔSLD2 (Fig. 4A; Supplemental Fig. S10A,B). The activity of SLD2 is likely linked to its ability to interact with UBC9, since the D394R mutant was as defective as ΔSLD2 in restoring normal cellular resistance to SUMO E1 inhibition. Similarly, while micronucleation after TAK-981 treatment in NFATC2IP-deficient cells could be completely rescued by expression of full-length epitope-tagged NFATC2IP, neither NFATC2IP D394R nor ΔSLD2 could do so (Fig. 4B; Supplemental Fig. S10B). Expression of NFATC2IP ΔSLD1 in *NFATC2IP*-KO cells also failed to suppress TAK-981-induced micronucleation but to a lesser degree than ΔSLD2 (Fig. 4B; Supplemental Fig. S10B). Together, these results indicate that NFATC2IP promotes genome integrity and cellular survival in response to SUMO E1 inhibition in a manner that requires both SLD1 and SLD2.

Despite the functional importance of the SUMO-like domains, we found that expression of SLD2 or a fragment encompassing SLD1–SLD2 was insufficient to restore re-

sistance of *NFATC2IP*-KO cells to SUMO E1 inhibition (Fig. 4C; Supplemental Fig. S10C,D), indicating that additional segments of the NFATC2IP protein contribute to its function. Therefore, to further dissect the structure–function relationship of NFATC2IP, we expressed protein deletion mutants (schematized in Supplemental Fig. S11) in *NFATC2IP*-KO cells and calculated their TAK-981 LD_{50} in clonogenic survival assays. From this analysis, we identified an additional region that contributes to NFATC2IP function in response to inhibition of SUMOylation that is encompassed within residues 101–140 (Fig. 4D; Supplemental Fig. S10E–H). Furthermore, our data suggest that most of the first 100 amino acid residues of NFATC2IP are dispensable for its role in promoting resistance to TAK-981.

The BTRR complex is essential in the absence of NFATC2IP

In parallel, we searched for genes that are selectively essential for the fitness of *NFATC2IP*-KO cells. We undertook parallel CRISPR screens in parental and *NFATC2IP*-KO cell lines with the TKOv3 sgRNA library and analyzed them with BAGEL2 (Kim and Hart 2021) and CRISP-RCount analysis (CCA) (Adam et al. 2021; Gallo et al. 2022) to identify genes that are selectively essential in the *NFATC2IP*-KO cell line (Fig. 5A; Supplemental Table S3). Among the top hits, *BLM* and *RMI2* (components of BTRR) were the sole genes encoding genome maintenance factors. Using two-color competition assays, we validated with two independent sgRNAs that RMI2 loss caused a pronounced loss of fitness in *NFATC2IP*-KO cells (Fig. 5B). Interestingly, depletion of RMI2 in parental cells increased micronucleation in response to TAK-981 (Fig. 5C), and its depletion in *NFATC2IP*-KO cells led to an additive increase in micronucleation (Fig. 5C), suggesting that NFATC2IP and BTRR promote genome integrity via parallel pathways.

NFATC2IP interacts with the SMC5/6 complex

The cell line dependency profile of *NFATC2IP* in DepMap (Dempster et al. 2019) showed correlation with those of *NSMCE2* and *SMC5*, encoding two components of the SMC5/6 complex (Supplemental Fig. S12; Supplemental Table S4). This relationship was notable because we were also struck by the similarities between the chromosome segregation phenotypes of *NFATC2IP*-KO cells following TAK-981 treatment and those of *SMC5*-, *SMC6*-, and *NSMCE2*-deficient cells (Gallego-Paez et al. 2014; Payne et al. 2014; Jacome et al. 2015; Pryzhkova and Jordan 2016). The SMC5/6 complex promotes proper chromosome segregation and genome integrity, with NSMCE2 acting as a SUMO E3 ligase associated with the complex (Potts and Yu 2005; Aragón 2018; Venegas et al. 2020). Since Esc2/Rad60 is also functionally linked with the SMC5/6 complex (Morishita et al. 2002; Sollier et al. 2009; Choi et al. 2010; Heideker et al. 2011; Prudden et al. 2011), we explored the possibility that NFATC2IP might mediate resistance to SUMOylation inhibition by
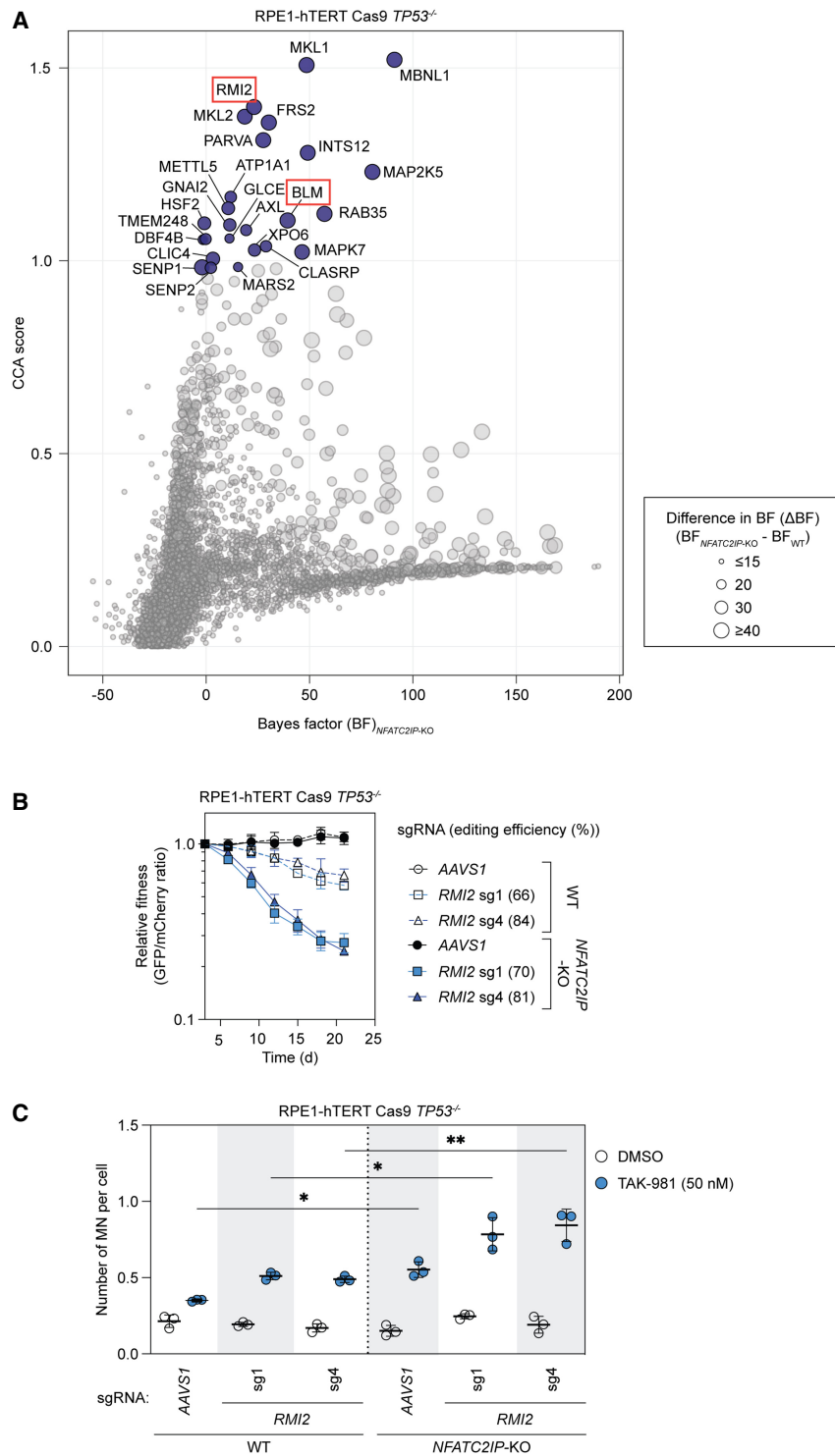
Figure 5. NFATC2IP acts in parallel with the BTRR complex to protect genome integrity. (*A*) Results of a dropout CRISPR screen in RPE1-hTERT Cas9 *TP53*$^{-/-}$ (WT) or isogenic *NFATC2IP*-KO cells. Genes that are highlighted with blue data points represent the top 25 hits from the CCA. (*B*) Two-color growth competition assays of cells expressing sgRNAs that target either *RMI2* or *AAVS1* (negative control) were done in RPE1-hTERT Cas9 *TP53*$^{-/-}$ (WT) or *NFATC2IP*-KO cells. Data are shown as the mean ± SD. (*n* = 3). The editing efficiency of *RMI2* targeting sgRNA1 and sgRNA4 was determined by TIDE analysis. (*C*) Quantitation of MN formation following treatment with either DMSO (vehicle) or 50 nM TAK-981 in RPE1-hTERT Cas9 *TP53*$^{-/-}$ (WT) or isogenic *NFATC2IP*-KO cells expressing the indicated sgRNAs. *AAVS1* sgRNA was used as a negative control. For each independent replicate, a minimum of 568 or 195 nuclei was counted in either WT or *NFATC2IP*-KO cells, respectively. Bars represent the mean ± SD. (*n* = 3). Multiple unpaired *t*-tests were performed for statistical comparison with Bonferroni–Dunn correction. (**) *P* < 0.01, (*) *P* < 0.05.

collaborating with the SMC5/6 complex, a relationship that is also consistent with the similar pattern of localization on nascent DNA described above.

To do so, we first surveyed the potential for protein–protein interactions between NFATC2IP and SMC5/6 complex members using AlphaFold-Multimer (Evans et al. 2021; Jumper et al. 2021; Mirdita et al. 2022) by testing pairwise combinations among NFATC2IP and SMC5/6

complex members, known SMC5/6 regulators that included SLF1, SLF2, and RAD18, as previously described (Supplemental Table S5; Sifri et al. 2023). This analysis recapitulated known protein–protein interactions in this complex, including the interaction between the BRCT domains of SLF1 and phosphorylatable residues in RAD18 (Räschle et al. 2015) or between the NSMCE3 subunit and NSMCE1 and NSMCE4 (Fig. 6A; Supplemental Table

S5; Adamus et al. 2020; Vondrova et al. 2020; Yu et al. 2021, 2022). With respect to NFATC2IP, AlphaFold-Multimer predicted an interaction with the SMC5 subunit of the SMC5/6 complex and NFATC2IP SLD1 (Fig. 6A,B; Supplemental Table S5). We validated these predictions in coimmunoprecipitation studies in 293T cells with 3xFLAG-tagged NFATC2IP variants and endogenous SMC5, which showed that the NFATC2IP–SMC5 interaction was absolutely dependent on SLD1 and, to a lesser ex-

tent, SLD2 (Fig. 6C). Furthermore, NFATC2IP interacts with UBC9 via its SLD2 (Prudden et al. 2009, 2011), raising the intriguing possibility that NFATC2IP makes contact with the SMC5/6-associated SUMO E3 ligase. We therefore carried out a new round of AlphaFold-Multimer predictions with NFATC2IP, UBC9, the coiled-coil region of SMC5, and NSMCE2 (Fig. 6D). A robust structural model was computed that was consistent with NFATC2IP SLD2 interacting with NSMCE2 through bridging by
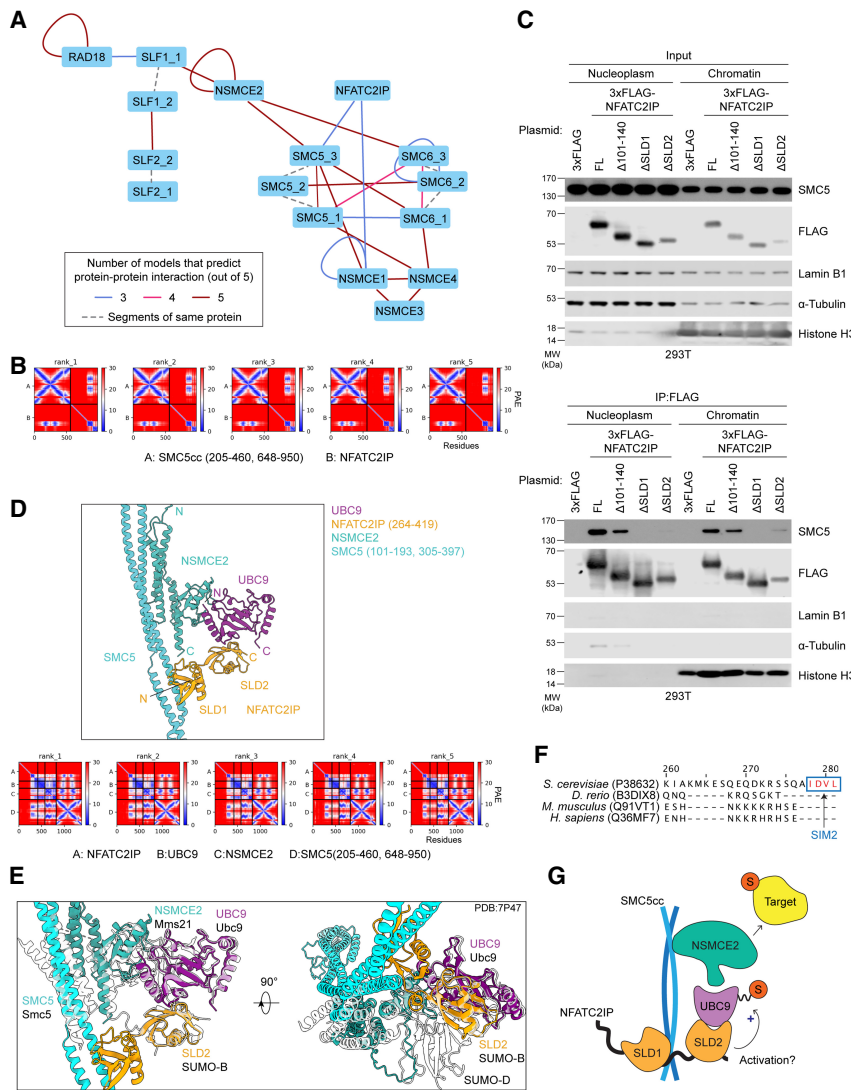

Figure 6. NFATC2IP binds the SMC5/6 complex through its SUMO-like domains. (A) Schematic of pairwise matrix screens by AlphaFold-Multimer to predict protein–protein interactions among NFATC2IP and the SMC5/6 complex subunits. Predicted interactions where at least three out of five models met the cutoff scores of pDockQ < 0.23 and interface predicted aligned error (PAE) < 15 Å are shown. Large proteins (SMC5, SMC6, SLF1, and SLF2) were divided into fragments according to either experimentally determined or AlphaFold-Multimer-predicted structural domain boundaries. Fragments of the same protein are indicated with dashed lines connecting the nodes. For SMC5, these are SMC5_1 ("head" region, residues 1–204 and 951–1101), SMC5_2 ("hinge" region, resides 461–647), and SMC5_3 ("coiled-coil" region, resides 205–460 and 648–950). For SMC6, these are SMC6_1 ("head" region, resides 1–201 and 952–1091), SMC6_2 ("hinge" region, residues 476–662), and SMC6_3 ("coiled-coil" region, residues 202–475 and 663–951 [derived from the human SMC5/6 complex structure]) (Adamus et al. 2020). For SLF1, these are SLF1_1 (residues 1–364) and SLF1_2 (residues 365–1058). For SLF2, these are SLF2_1 (residues 1–600) and SLF2_2 (residues 601–1173). (B) PAE plots of the interaction between the coiled-coil region of SMC5 (SMC5_3 fragment of the pairwise modeling) and NFATC2IP, ranked by predicted template model (pTM) scores. (C) Subcellular fractions of 293T cells transiently expressing the indicated 3xFLAG-tagged NFATC2IP constructs were subjected to immunoprecipitation with anti-FLAG antibodies. Input samples and immunoprecipitation products were immunoblotted with the indicated antibodies. α-Tubulin, lamin B1, and histone H3 were included as controls for cytoplasmic, nucleoplasmic, and chromatin subcellular fractionations, respectively. (FL) Full-length. (D, top panel) Representative model of the AlphaFold-Multimer predictions of protein–protein interactions among the NFATC2IP SLDs (yellow), NSMCE2 (sea green), UBC9 (purple), and a portion of the SMC5cc region (cyan). (Bottom panel) The PAE plots of the prediction models associated with the top panel. (E) Overview of the representative AlphaFold-Multimer prediction model (colors are as in D) overlaid with the structure of the Smc5/Nse2 complex with the Ubc9~SUMO mimetic (PDB: 7P47; translucent). Proteins in the crystal structure are indicated alongside the AlphaFold-Multimer model at corresponding positions. (F) Multiple sequence alignment of amino acid sequences of the human NSMCE2 protein (Homo sapiens) and its orthologs in S. cerevisiae, zebrafish (Danio rerio), and mice (Mus musculus) with the associated UniProt entry codes and amino acid positions using the Clustal Omega sequence alignment tool. Amino acid residues of the SUMO-interacting motif (SIM2) on the C-terminal end of Nse2 for positioning backside SUMO in yeast are highlighted with a blue box and red text. (G) Functional model of the NFATC2IP–SMC5/6–NSMCE2–UBC9 complex. The arrow indicates the potential positive regulation of NSMCE2-dependent SUMOylation by NFATC2IP.

UBC9, which interacts with NFATC2IP and NSMCE2 through two distinct interfaces (Fig. 6D). Interestingly, SLD2 binds to UBC9 on the same "backside" site on UBC9 that is known to bind a SUMO molecule. In yeast, the binding of SUMO on the Ubc9 backside site plays a key role in stimulating the E3 ligase activity of Nse2 by stimulating the discharge of the Ubc9∼SUMO thioester intermediate (Fig. 6E; Varejão et al. 2021). However, in yeast, the backside SUMO is positioned by a SUMO-interacting motif (SIM) on Nse2 (Varejão et al. 2021) that is absent in mammalian NSMCE2 (Fig. 6F), suggesting that NSMCE2 is unable to bind SUMO and activate UBC9 using as similar mechanism. Instead, we propose that in mammalian species, it is SLD2 of NFATC2IP that occupies the backside of UBC9 to activate NSMCE2 activity (Fig. 6E). Therefore, our genetic, interaction, and modeling data suggest that NFATC2IP acts as a positive regulator of SUMOylation by the SMC5/6 complex (Fig. 6G).

NFATC2IP promotes chromatin SUMOylation

To investigate whether loss of NFATC2IP affects the levels of SUMOylation in cells, parental and *NFATC2IP*-KO cells were transduced with a plasmid stably expressing either His$_6$-SUMO1 or His$_6$-SUMO2. SUMOylated proteins were purified from cell lysates using nickel–nitrilotriacetic acid (Ni-NTA) agarose beads in strong denaturing conditions, and global SUMOylation levels were monitored by immunoblotting with antibodies to SUMO1 (Fig. 7A) or SUMO2/3 (Fig. 7B). As control for the affinity purification, we monitored RanGAP1, which is a well-characterized SUMOylated protein (Matunis et al. 1996). We found that in contrast to the abundance of SUMO1-modified proteins, which showed no difference in the pull-downs from the lysates derived from parental (WT) and *NFATC2IP*-KO cells (Fig. 7A), there was a noticeable decrease in the amount of high-molecular-weight SUMO2/3-modified proteins pulled down from *NFATC2IP*-KO cells compared with those purified from parental cells (Fig. 7B). The same was seen for SUMO2/3-modified RanGAP1 (Fig. 7B). These data suggested that NFATC2IP may promote SUMOylation of proteins primarily by SUMO2/3.

Since the above experiments relied on overexpression of exogenous SUMO proteins, we next assessed whether NFATC2IP promotes SUMOylation under endogenous conditions. To do so, we subfractionated lysates of parental and *NFATC2IP*-KO cells and isolated SUMOylated proteins using a biotinylated S-Cap peptide that has high affinity for SUMOylated proteins. With this approach, we observed a large decrease in the amount of high-molecular-weight SUMO2/3-modified proteins specifically in the chromatin fraction of *NFATC2IP*-KO cells (Fig. 7C), with no difference observed in the amount of SUMO2/3-modified proteins retrieved from either the nucleoplasmic or cytoplasmic fractions (Supplemental Fig. S13). This defect in chromatin SUMOylation seen in *NFATC2IP*-KO cells was fully rescued by re-expression of 3xFLAG-NFATC2IP but not the ΔSLD1, ΔSLD2, and D394R mutants, indicating that this phenotype correlates with the viability of cells fol-

lowing SUMO E1 inhibition (Fig. 7D). Intriguingly, analysis of the proteins retrieved by the S-Cap peptide by mass spectrometry did not identify differentially SUMOylated proteins in *NFATC2IP*-KO cells (Supplemental Table S6). This may suggest that NFATC2IP promotes the extent of SUMOylation rather than modulating the initial SUMOylation of substrates. This is consistent with SUMO2/3 being the main SUMO isoform that composes poly-SUMO chains (Vertegaal 2022). Together, these data indicate that NFATC2IP promotes SUMOylation of chromatin-associated proteins by stimulating the SUMO E3 ligase activity of the SMC5/6 complex.

Discussion

We report the identification of 130 genes that promote the viability of human RPE1-hTERT *TP53*$^{-/-}$ cells when facing SUMO E1 inhibition. We focused our subsequent validation and mechanistic studies on *NFATC2IP*, since its disruption showed a large effect size with respect to sensitization to TAK-981 in our cell line. These results place NFATC2IP as a key mediator of the response of human cells to SUMO E1 inhibition.

While the developers of TAK-981 have highlighted its potential to stimulate antitumor immunity (Lightcap et al. 2021), we found that the intrinsic sensitivity of cells to SUMO E1 inhibition is largely driven by a few pathways that include genome maintenance and transcriptional regulation (Supplemental Fig. S1B). With respect to genome maintenance, in addition to NFATC2IP, our screen identified genes encoding factors known to be involved in the resolution of recombination intermediates, such as components of the BLM–RMI1–RMI2–TOP3A complex, GEN1, and the SMC5/6 complex. This is not entirely surprising given the key role of SUMO in controlling recombination in yeast (Ulrich et al. 2005; Branzei et al. 2006; Psakhye and Jentsch 2012). Our studies are consistent with a model in which NFATC2IP resolves either recombination intermediates or topological entanglements by promoting the activity of the SUMO E3 ligase associated with the SMC5/6 complex. We propose that under conditions of limiting SUMOylation, the essential activity of the SMC5/6-associated NSCME2 E3 ligase for chromosome stability becomes highly dependent on NFATC2IP-mediated stimulation.

The model that NFATC2IP acts to stimulate SMC5/6-dependent SUMOylation is supported by a number of converging lines of evidence. First, there is a clear correlation between *NFATC2IP* and a subset of genes encoding SMC5/6 complex members in DepMap. Second, the loss of SMC5/6 or NSMCE2 produces a chromosome-bridging phenotype that is nearly identical to the phenotype observed in *NFATC2IP*-KO cells treated with TAK-981. Third, NFATC2IP interacts physically with SMC5 and UBC9 via its two SLDs, which are themselves required for promoting chromosome integrity and survival following SUMO E1 inhibition. The physical interaction between NFATC2IP, SMC5, and UBC9 can be rationalized with an AlphaFold-Multimer-generated structural model that
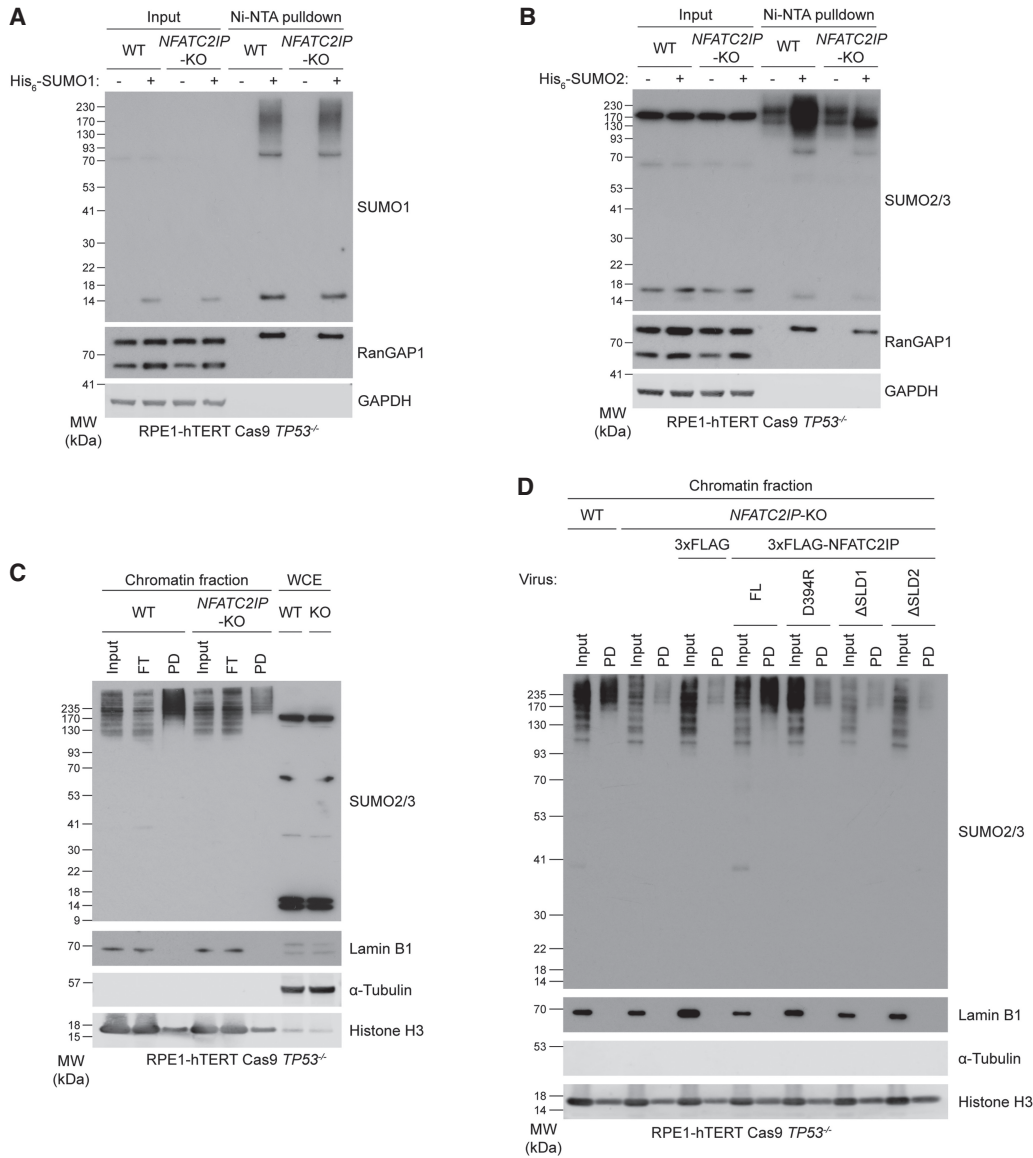
Figure 7. NFATC2IP promotes SUMOylation in chromatin. (*A,B*) Immunoblot analysis of whole-cell extracts of parental RPE1-hTERT Cas9 $TP53^{-/-}$ (WT) or isogenic *NFATC2IP*-KO cells that were transiently transfected with plasmids for overexpression of His$_6$-SUMO1 (*A*) or His$_6$-SUMO2 (*B*), followed by purification of His-tagged peptides using Ni-NTA agarose beads under denaturing conditions. The immunoblots were probed with antibodies to the indicated proteins. RanGAP1 was used as a SUMOylation control. GAPDH was used as a loading control. (*C*) Immunoblot analysis of chromatin subfractions of extracts derived from parental RPE1-hTERT Cas9 $TP53^{-/-}$ (WT) or isogenic *NFATC2IP*-KO cells. SUMO-conjugated proteins were isolated by binding to the biotinylated S-Cap peptide, followed by affinity pull-down with streptavidin-conjugated magnetic beads. (Input) Input control fraction, (FT) unbound flow-through after binding of biotin S-Cap to streptavidin beads, (PD) proteins from S-Cap pull-down eluted from streptavidin beads, (WCE) whole-cell extract. Immunoblots were probed using antibodies to the indicated proteins. α-Tubulin, lamin B1, and histone H3 were included as controls for cytoplasmic, nucleoplasmic, and chromatin subcellular fractions, respectively. (*D*) Immunoblot analyses of chromatin subfractions of extracts derived from parental RPE1-hTERT Cas9 $TP53^{-/-}$ (WT) or isogenic *NFATC2IP*-KO cells that either were left untransduced or were transduced with a lentivirus encoding the indicated protein. The subfractionated chromatin extracts were subjected to isolation of SUMO-conjugated proteins via binding to the biotinylated S-Cap peptide, followed by affinity pull-down with streptavidin-conjugated magnetic beads. (Input) Input control fraction before binding to streptavidin-conjugated magnetic beads, (PD) proteins from S-Cap pull-down eluted from streptavidin beads, (WCE) whole-cell extract. Immunoblots were probed using antibodies to the indicated proteins. α-Tubulin, lamin B1, and histone H3 were included as controls for cytoplasmic, nucleoplasmic, and chromatin subcellular fractions, respectively.

suggests that NFATC2IP acts to stimulate the discharge of UBC9~SUMO. Interestingly, in addition to SLD1/2, we identified another region essential for NFATC2IP action lo-

cated within residues 101–140. The molecular function of this region remains unclear, as it was not modeled to interact with any other member of the SMC5/6 pathway.

However, we note that NFATC2IP homologs have been shown to display DNA-binding activity that maps N-terminal of SLD1/2 (Urulangodi et al. 2015; Sebesta et al. 2017). Whether this region in NFATC2IP also confers DNA-binding activity is currently unknown but represents an attractive starting point for future studies.

While we were completing these studies, Hertz et al. (2023) also reported that NFATC2IP (referred to as NIP45) was essential to promote normal cellular resistance to SUMO E1 inhibition. While the studies are largely concordant in that they both identify chromosome nondisjunctions as a likely source for the lethality of NFATC2IP-deficient cells under conditions of limiting SUMOylation, the studies differ in how those chromosome entanglements are generated. While Hertz et al. (2023) propose an E3-like activity for NFATC2IP that targets SLX4 and possibly other proteins in the resolution of double-stranded DNA catenanes during M phase, our data instead link NFATC2IP to the SUMO E3 ligase activity of the SMC5/6 complex. We also present evidence that NFATC2IP acts during interphase, a finding that is supported by both the observation that NFATC2IP-KO cells treated with TAK-981 have defective incorporation of the EdU nucleoside during S phase and observation that NFATC2IP is in proximity to nascent DNA, as is SMC5. Interestingly, the SMC5/6 complex similarly promotes DNA replication, and this activity represents its essential function, which is key to preventing chromosome aberrations and bridging during mitosis (Gallego-Paez et al. 2014; Venegas et al. 2020; Peng and Zhao 2023). On balance, we contend that the genetic, physical, and phenotypic links between NFATC2IP and SMC5/6 are compelling enough to further test this model in future studies. However, this work certainly does not exclude the possibility that NFATC2IP may have other SUMO-related activities, such as stimulating SLX4 SUMOylation.

Finally, given that the phenotypes of NFATC2IP-KO cells treated with low doses of the SUMO E1 inhibitor are remarkably similar to the phenotypes associated with mutations in SMC5/6 or associated proteins (Gallego-Paez et al. 2014; Payne et al. 2014; Jacome et al. 2015; Pryzhkova and Jordan 2016), it may be of interest to screen for NFATC2IP mutations in patients that display chromosome breakage disorders linked to the SMC5/6 complex such as Atelis, Seckel, and LICS syndromes, associated with SMC5, SLF2, NSMCE2, and NSMCE3, respectively. However, as the NFATC2IP-KO cellular phenotypes are only uncovered when SUMOylation is inhibited, we expect that the phenotypes associated with loss of NFATC2IP will be milder than those seen with mutations in SMC5/6 complex-coding genes or will affect tissues that have lower levels of SUMOylation than our model cell line.

Materials and methods

Cell lines and cell culture

RPE1-hTERT Cas9 TP53-KO and 293T cell lines were cultured in Dulbecco's modified Eagle medium (DMEM; Gibco 11965092) supplemented with 10% (v/v) FBS (Wisent Bio-

products 080-150) and 1% (v/v) penicillin/streptomycin (Wisent Bioproducts 450-201-EL) and grown at 37°C and 5% CO_2. The clonal RPE1-hTERT Cas9 $TP53^{-/-}$ NFATC2IP-KO cell lines were generated by transfecting a ribonucleoprotein (RNP) complex of the NFATC2IP targeting sgRNA2 (Supplemental Table S7) and purified Cas9 protein into RPE1-hTERT Cas9 $TP53^{-/-}$ cells using Lipofectamine CRISPRMAX Cas9 transfection reagent (Invitrogen CMAX00003). Transfection of the RNP complex was performed according to the manufacturer's protocol for 24 h, and the transfected pool of cells was seeded for clonal isolations. The selected NFATC2IP-KO clones were validated for successful gene editing by TIDE analysis (Brinkman et al. 2014) and by probing for endogenous NFATC2IP protein levels by immunoblotting.

Plasmids

For CRISPR-mediated gene disruption, DNA oligonucleotides containing sgRNAs were cloned (using BsmBI) into LentiCRISPRv2 (Addgene 52961) or a modified LentiGuide-Puro (Addgene 52963) that was altered to include an expression cassette of nuclear localization signal (NLS)-fused GFP or mCherry (Sanjana et al. 2014; Noordermeer et al. 2018). To generate NFATC2IP-expressing plasmids, a plasmid containing the human NFATC2IP cDNA was purchased from the Lunenfeld-Tanenbaum Research Institute OpenFreezer repository (OpenFreezer ID V84563). The NFATC2IP-coding sequence was amplified by PCR with primers containing flanking AscI and EcoRV restriction sites and cloned into pcDNA5-FRT/TO-FLAG, pcDNA5-FRT/TO-eGFP, and pcDNA5-FRT/TO-3×FLAG for N-terminal epitope tagging. To generate plasmids expressing NFATC2IP mutants, site-directed mutagenesis was performed via PCR. To generate plasmids expressing NES-fused or NESm-fused NFATC2IP, DNA fragments encoding NES or NESm sequences were inserted into NFATC2IP-cloned pcDNA5-FRT/TO-3xFLAG or pcDNA5-FRT/TO-eGFP vectors using AscI. The sequences encoding 3xFLAG-tagged or eGFP-tagged NFATC2IP were then PCR-amplified with primers containing flanking NotI and XbaI restriction sites and cloned into the pHIV-NAT-T2A-hCD52 lentiviral vector (a kind gift from Dr. R. Scully). To generate plasmids for expressing SPR degron-tagged NFATC2IP, the coding sequence of eGFP-tagged NFATC2IP was PCR-amplified with flanking EcoRV restriction sites. The EcoRV digestion product was used to replace mNeonGreen in AAVS1_Puro_PGK1_mNG_hGEM(1–110)-GGGS-hSLBP (18–108)-BGHpA, which will be deposited soon at Addgene (gift from Y Doyon). The sequence encoding SPR degron-fused eGFP-NFATC2IP was then cloned into the pHIV-NAT-T2A-hCD52 lentiviral vector as described above using flanking EcoRI and XbaI restriction sites.

Lentiviral transduction

To produce lentivirus, 4×10^6 293T cells were seeded in a 10-cm plate 1 d prior to transfection and cotransfected with the third-generation lentiviral packaging plasmids (5 µg of

pVSV.G, 3 µg of pMDLg/pRRE, and 2.5 µg of pRSV-Rev; Addgene 14888, 12251, and 12253, respectively) plus 10 µg of the vector of interest using Mirus TransIT-LT1 transfection reagent (Mirus Bio LLC MIR 2305). Medium was refreshed 16 h after transfection, and the viral supernatant was collected ~36–40 h after transfection and passed through a 0.45-µm filter. For infection of target cells, the viral supernatant was supplemented with 8 µg/mL polybrene (Sigma H9268). For selection of transduced RPE1-hTERT Cas9 *TP53*$^{-/-}$ WT or *NFATC2IP*-KO cells, cells were grown in media containing 1.5 µg/mL puromycin (Life Technologies A1113802) for 48 h or 400 µg/mL nourseothricin (NAT; Gold Biotech N-500) for 4–5 d.

CRISPR/Cas9 screens

The chemogenomic CRISPR screen was performed as described by Olivieri and Durocher (2021). Briefly, RPE1-hTERT Cas9 *TP53*$^{-/-}$ cells were transduced with the TKOv3 lentiviral sgRNA library (Hart et al. 2017) at a multiplicity of infection (MOI) of ~0.3 and selected with 1.5 µg/mL puromycin (Life Technologies A1113802) for 48 h. The pooled population of transduced cells was subcultured every 3 d in two technical replicates until 6 d after selection (t6). At the t6 time point, the subpopulations of cells were either exposed to DMSO (vehicle; Sigma D2650) as a nontreated control or treated with the SUMO E1 inhibitor TAK-981 (Chemietek CT-TAK981) for 12 d at the dosages described in Supplemental Table S1. Cells were harvested at the t18 time point, genomic DNA was purified using the QIAmp DNA Blood Maxi kit (Qiagen 51194), and the integrated sgRNA sequences were amplified and barcoded by two-step PCR using NEB-Next Ultra II Q5 master mix (New England Biolabs M5044). The barcoded sgRNA samples were sequenced on an Illumina NextSeq500 to quantitate representation of each sgRNA in the TAK-981-treated or nontreated control samples. As described previously, the gene-level normZ scores were computed using DrugZ from the read counts (Supplemental Table S1; Colic et al. 2019).

For dropout CRISPR screens, RPE1-hTERT Cas9 *TP53*$^{-/-}$ (WT) or isogenic *NFATC2IP*-KO cells were transduced with the TKOv3 lentiviral sgRNA library at a MOI of ~0.3 and subjected to puromycin selection (1.5 µg/mL) for 48 h. A portion of the transduced cell populations was harvested for the initial time point (t0), and the remaining cells were subcultured every 3 d in two technical replicates until t18. The cell populations that were harvested at the t0 and t18 time points were subjected to genomic DNA purification and amplification as well as barcoding of the integrated sgRNA sequences as described above. The barcoded sgRNAs were sequenced on an Illumina NextSeq500 to determine representation of each sgRNA in the t0 and t18 time-point samples. The gene-level comparisons of essentialities in RPE1-hTERT Cas9 *TP53*$^{-/-}$ or isogenic *NFATC2IP*-KO cells were performed by computing the Bayes factor and CCA score for each gene as described previously (Supplemental Table S3; Adam et al. 2021; Kim and Hart 2021),

Clonogenic survival assays

For clonogenic survival assays with TAK-981, cells were seeded in media containing a range of TAK-981 concentrations at a seeding density of 400 cells per 10-cm plate. TAK-981-containing media were refreshed every 4 d, and cells were grown for 14 d. Cells were then rinsed with DPBS (Gibco 14190144) and stained with 0.5% (w/v) Crystal Violet/20% methanol (Crystal Violet; Sigma C0775) for 30 min. The numbers of colonies formed were counted by image analysis using GelCount (Oxford Optronix), and the relative surviving fractions were plotted by normalizing to DMSO controls.

Antibodies

Primary antibodies used in this study for immunoblotting, immunofluorescence (IF), flow cytometry, or proximity ligation assay in SIRF (PLA/SIRF) were as follows: rabbit anti-GAPDH (1:10,000 for immunoblotting; Sigma G9545), mouse anti-NFATC2IP (B-1, 1:100 for immunoblotting; Santa Cruz Biotechnology sc-377461), rabbit anti-GFP (1:1000 for immunoblotting and 1:100 for PLA/SIRF; Abcam ab290), mouse anti-α-tubulin (DM1A, 1:2000 for immunoblotting; Cell Signaling Technologies 3873), mouse anti-α-actinin (AT6/172, 1:2000 for immunoblotting; Millipore 05-384), anticentromere protein antibody (ACA; 1:1000 for IF; Antibodies Incorporated 15-235), rat anti-FLAG (L5, 1:500 for IF; BioLegend 637301), mouse anti-FLAG M2 (1:500 for immunoblotting; Sigma F1804), rabbit anti-phospho-histone H2A.X Ser139 (1:1000 for flow cytometry; Cell Signaling Technologies 2577), mouse anti-phospho-histone H3 Ser10 (6G3, 1:500 for flow cytometry; Cell Signaling Technologies 9706), mouse anti-cyclin A (B-8, 1:500 for immunoblotting; Santa Cruz Biotechnology sc-271682), mouse anti-cyclin E1 (HE12, 1:1000 for immunoblotting; Abcam ab3927), mouse antibiotin (BN-34, 1:100 for PLA/SIRF; Sigma SAB4200680), rabbit antibiotin (D5A7, 1:100 for PLA/SIRF; Cell Signaling Technologies 5597), rabbit anti-SMC5 (1:400 for immunoblotting and 1:200 for PLA/SIRF; Novus Biologicals NB100-469), mouse anti-PCNA (PC10, 1:100 for PLA/SIRF; Abcam ab29), rabbit anti-RanGAP1 (EPR3295, 1:2000 for immunoblotting; Abcam ab92360), rabbit anti-SUMO1 (Y299, 1:1000 for immunoblotting; Abcam ab32058), rabbit anti-SUMO2/3 (1:1000 for immunoblotting; Abcam ab3742), rabbit anti-lamin B1 (1:1000 for immunoblotting; Abcam ab16048), and rabbit anti-histone H3 (1:4000 for immunoblotting; Abcam ab1791).

For immunoblotting, the following secondary antibodies were used: horseradish peroxidase (HRP)-conjugated AffiniPure goat antimouse IgG (H+L, 1:5000; Jackson ImmunoResearch Laboratories, Inc. 115-035-003), HRP-conjugated AffiniPure goat antirabbit IgG (H+L, 1:5000; Jackson ImmunoResearch Laboratories, Inc. 111-035-144), IRDye 680RD donkey antimouse IgG (1:5000; LI-COR Biosciences 926-68072), IRDye 680RD goat antimouse IgG (1:5000; LI-COR Biosciences 926-68070), and

IRDye 800CW donkey antirabbit IgG (1:5000; LI-COR Biosciences 926-32213).

For immunofluorescence, the secondary antibodies used in this study included the following: Alexa fluor 555 goat antirabbit IgG (H+L, 1:1000; Invitrogen A21428), Alexa fluor 555 goat antirat IgG (H+L, 1:1000; Invitrogen A21434), Alexa fluor 647 goat antirabbit IgG (H+L, 1:1000; Invitrogen A21244), Alexa fluor 647 goat antimouse IgG (1:1000; Invitrogen A21236), and Alexa fluor 488 goat antihuman IgG (H + L, 1:1000; Invitrogen A11013).

For flow cytometry, the following secondary antibodies were used: Alexa fluor 488 goat antirabbit IgG (H+L, 1:1000; Invitrogen A11034) and Alexa fluor 555 goat antimouse IgG (H+L, 1:1000; Invitrogen A21424).

Immunofluorescence

Cells were seeded on glass coverslips and subjected to various treatments detailed elsewhere. For experiments involving incorporation of EdU (5-ethynyl-2′-deoxyuridine; Life Technologies A10044), cells were incubated with media containing 20 µM EdU in DMSO for 20 min before harvesting. Cells on glass coverslips were washed with DPBS and fixed with 4% (w/v) formaldehyde/DPBS (16% [w/v] formaldehyde [Pierce], methanol-free [Thermo Fisher 28908], diluted in DPBS) for 15 min and then permeabilized with 0.3% (v/v) Triton X-100/DPBS (Sigma T8787) for 30 min. Cells were incubated with PBG blocking buffer (0.2% fish gelatin [Sigma G7765], 0.5% [w/v] bovine serum albumin [BSA; Roche 10735094001] diluted in DPBS) for 30 min and then with primary antibodies diluted in PBG blocking buffer for 1–2 h. Following three washes with PBS, cells were incubated with PBG blocking buffer containing secondary antibodies and 0.4 µg/mL DAPI (4′,6-diaminido-2-phenylindole; Sigma D9542) for 1 h and then washed three times with DPBS. Cells were mounted onto glass slides using ProLong Gold Antifade mountant (Thermo Fisher P36930) and imaged on a Zeiss LSM780 confocal microscope.

Quantitation of micronucleus formation

Cells were seeded in 96-well plates at a seeding density of 3000 cells per well 24 h prior to the TAK-981 treatment. Cells were treated with TAK-981 for 48 h, followed by fixation with 4% (w/v) formaldehyde/DPBS for 15 min and permeabilization with 0.3% (v/v) Triton X-100/DPBS for 30 min. Cells were rinsed with DPBS and incubated for 30 min with blocking buffer (5% [w/v] BSA, 0.1% [v/v] Tween-20 [10% Tween-20 solution; Bio-Rad 1610781] diluted in DPBS). Cells were incubated with primary antibodies diluted in blocking buffer for 2 h, followed by three washes with PBT (0.1% [v/v] Tween-20/DPBS). Subsequently, cells were incubated with the blocking buffer containing secondary antibodies as listed above and 0.4 µg/mL DAPI. After three final washes with PBT and one wash with DPBS, 200 µL of DPBS was added to each well. Plates were scanned for image acquisitions on an InCell Analyzer 6000 automated microscope (GE Healthcare) with a 20× or 60×

objective. Image analyses for micronucleus quantitation were performed using Columbus image storage and analysis software (Perkin Elmer).

Quantitation of chromatin bridge formation

Cells were seeded in six-well plates with glass coverslips at a seeding density of 150,000–200,000 cells per well 24 h prior to the TAK-981 treatment. Media containing a range of TAK-981 concentrations were added to the cells and incubated for 24 h. Cells were fixed with 4% (w/v) formaldehyde/DPBS for 15 min, blocked with PBG blocking buffer (as described above) for 30 min, and incubated in blocking buffer containing 0.8 µg/mL DAPI for 1 h. Cells were then mounted onto glass slides using ProLong Gold Antifade mountant and imaged on a Zeiss LSM780 confocal microscope. For quantitation of chromatin bridges, 300–500 nuclei per condition were observed and categorized according to the presence and length of chromatin bridges and then used to calculate the proportions of nuclei displaying short or long chromatin bridges.

Flow cytometry

Cells were seeded in 10-cm plates and subjected to various treatments as indicated elsewhere. Prior to harvesting samples, cells were pulsed with 20 µM EdU in DMSO for 30 min. Cell pellets were collected by trypsinization and washed once with DPBS. Cells were fixed with 4% (w/v) formaldehyde/PBS for 15 min at room temperature and washed with ice-cold PBS-B (1% BSA in DPBS, sterilized with 0.22-µm filter) by pelleting cells at 600g for 3 min at 4°C. The fixed cells were permeabilized with 0.5% (v/v) Triton X-100/PBS-B for 30 min at room temperature and then washed with ice-cold PBS-B. For the Click reaction of incorporated EdU, cells were resuspended in EdU staining buffer (150 mM Tris-HCl at pH 8.50, 2 mM CuSO$_4$ [BioShop Life Science Products CUS803.500], 100 mM L-ascorbic acid [Sigma A5960], 10 µM Alexa fluor 647 azide [Life Technologies A10277]), incubated for 1 h at room temperature in the dark, and washed twice with blocking buffer (PBS-B supplemented with 0.1% NP-40 [Sigma I3021]). The cells were stained with primary antibodies diluted in blocking buffer for 1 h at room temperature, protected from light, and then washed with PBS-B. The cells were then stained by incubation in blocking buffer containing secondary antibodies as listed above for 1 h at room temperature in the dark. Following washes with blocking buffer, cell pellets were resuspended in analysis buffer (0.5 µg/mL DAPI, 250 µg/mL RNase A [Sigma R4875] in PBS-B) and incubated for 16–24 h at 4°C in the dark. Cells were analyzed on a Attune NxT flow cytometer (Thermo Fisher) by measuring a minimum of 19,631 events and were visualized using FlowJo v10 (BD Biosciences).

SIRF assay

Proximity ligation assays for SIRF analysis were performed as described previously by Roy et al. (2018) and Roy and Schlacher (2019). Briefly, cells were seeded at a

density of 40,000 cells per well onto eight-well chamber microscope slides (Thermo Fisher 177402) 1 d prior to the experiment. Cells were pulsed with either DMSO as a negative control or 125 µM EdU for 8 min. For thymidine chase, following the EdU pulse, cells were washed twice with DPBS and incubated in media containing 100 µM thymidine (Sigma T9250) for 6 h. After two washes with DPBS, cells were fixed with 4% (w/v) formaldehyde/PBS for 15 min at room temperature and again washed twice with DPBS. After fixation, cells on the slides were permeabilized with 0.25% Triton X-100/DPBS in Coplin jars for 15 min at room temperature, followed by two washes with DPBS for 5 min each. For conjugation of biotin to EdU, Click reaction cocktail (150 mM Tris-HCl at pH 8.50, 2 mM CuSO$_4$, 10 mM L-ascorbic acid, 5 µM Alexa fluor 647 azide, 5 µM biotin azide [PEG4 carboxamide-6-azidohexanyl biotin; Invitrogen B10184]) was added to slides, incubated in a humidified chamber for 1.5 h at room temperature, and washed with DPBS for 5 min. Slides were then incubated in blocking buffer (10% goat serum [Sigma G6767], 0.1% Triton X-100 in DPBS) in a humidified chamber for 1 h at room temperature, followed by incubation with primary antibodies diluted in blocking buffer in a humidified chamber overnight at 4°C. Primary antibodies recognizing either PCNA, GFP, or SMC5 (listed above) were used together with mouse or rabbit antibodies targeting biotin. Slides were washed three times in Coplin jars with Duolink in situ wash buffer A (Sigma DUO82049) for 5 min each. Slides were incubated with the Duolink in situ PLA probes antimouse Plus (Sigma DUO92001) and antirabbit Minus (Sigma DUO92005), which were diluted at a 1:5 ratio in blocking buffer for 1 h at 37°C in a humidified chamber, and then washed three times with Duolink in situ wash buffer A for 5 min each. For ligation and amplification steps described below, the reagents used were included in the Duolink in situ detection reagent Red kit (Sigma DUO92008). Slides were incubated with ligation reaction mixture (1× ligation buffer, 1 U of ligase diluted in H$_2$O) for 30 min at 37°C in a humidified chamber and washed twice with Duolink in situ wash buffer A for 2 min each. For amplification, slides were incubated with amplification reaction mixture (1× amplification buffer, 5 U of polymerase diluted in H$_2$O) for 100 min at 37°C in a humidified chamber. Slides then were washed three times with Duolink in situ wash buffer B (Sigma DUO82049) for 10 min each and once with 0.01× Duolink in situ wash buffer B diluted in H$_2$O for 1 min. Slides were stained with 1 µg/mL DAPI prepared in DPBS for 15 min at room temperature in a humidified chamber and washed twice with DPBS for 5 min each. DAPI-stained slides were mounted using glass coverslips (Epredia 22-050-232) and Prolong Gold Antifade mountant and cured overnight in the dark. Cells were imaged on a Zeiss LSM780 confocal microscope and analyzed using CellProfiler software (Stirling et al. 2021).

AlphaFold-Multimer pairwise matrix screen

Amino acid sequences for human NFATC2IP, SMC5, SMC6, NSMCE1, NSMCE2, NSMCE3, NSMCE4, SLF1, SLF2, and RAD18 were obtained from UniProt. For proteins with >1000 residues, their amino acid sequences were manually divided into smaller fragments as described elsewhere due to limited graphical memory. As previously described (Sifri et al. 2023), as input for AlphaFold-Multimer prediction, FASTA files for every unique pair were generated using a Python script. For each prediction of protein–protein interaction, the confidence was analyzed by computing pDockQ (Bryant et al. 2022) and mean interface PAE values. To determine mean interface PAE, every pair of residues was identified as described by Sifri et al. (2023), and PAE value was measured for each residue pair. The average PAE value was then computed across all pairs of residues. High-confidence predictions of protein interactions were identified by filtering for unique pairs where at least three out of five prediction models met the cutoff values of pDockQ < 0.23 and interface PAE < 15 Å. UCSF ChimeraX software was used for visualizing protein structures (Goddard et al. 2018).

Subcellular fractionation

Cells were plated in 15-cm plates, and the harvested cells were subjected to subcellular fractionation as described previously (Fradet-Turcotte et al. 2013). Briefly, cells were lysed in EBC1 buffer (50 mM Tris-HCl at pH 7.50, 100 mM NaCl, 0.5% NP-40, 1 mM EDTA, 1 mM DTT, 1× protease inhibitor cocktail [cOmplete mini, EDTA-free; Roche 11836170001], 5 mM N-ethylmaleimide [NEM; Sigma E1271]). The nuclear fraction (pellet) was separated from the cytoplasmic fraction (supernatant) by centrifugation at 1000g for 10 min at 4°C. The nucleoplasmic fraction was obtained by resuspending the nuclear pellet in EBC2 buffer (50 mM Tris-HCl at pH 7.50, 300 mM NaCl, 5 mM CaCl$_2$, 1× protease inhibitor cocktail, 5 mM NEM) for 30 min on ice with occasional vortexing, after which the soluble nucleoplasmic fraction (supernatant) was separated from the insoluble chromatin (pellet) by centrifugation at 21,000g for 10 min at 4°C. The insoluble chromatin pellets were then solubilized in EBC2 buffer supplemented with 10 U of micrococcal nuclease (Sigma N3755) per 15-cm plate by digestion for 45 min at 30°C. The soluble chromatin fraction samples were harvested by centrifugation at 21,000g for 10 min at 4°C, and the supernatant was collected.

Immunoprecipitation

293T cells were seeded in 10-cm plates and transfected with the plasmids expressing the NFATC2IP protein constructs that were cloned into pcDNA5-FRT/TO-3xFLAG parental vectors using Mirus TransIT-LT1 transfection reagent (Mirus Bio LLC MIR 2305). Twenty-four hours after transfection, the transfection mix was removed, and cells were allowed to recover in fresh media for another 24 h before harvesting. Cells were then subjected to subcellular fractionation into cytoplasmic, nucleoplasmic, or chromatin extracts as described above except that DTT was omitted from the EBC1 buffer. For immunoprecipitations of FLAG-tagged peptides, protein concentrations in

samples from each subfraction were normalized and subjected to binding of FLAG-tagged polypeptide species with anti-FLAG M2 magnetic beads (Sigma M8823). The input controls were collected prior to the incubation with anti-FLAG M2 magnetic beads. The purified FLAG-tagged polypeptides were harvested by eluting from the anti-FLAG M2 magnetic beads with 100 ng/µL 3xFLAG peptides (GlpBio GP10149-1).

Purification of 6xHis-tagged SUMO-conjugated peptides

Cells were plated in 10-cm plates and transfected with plasmids expressing His$_6$-SUMO1 (Addgene plasmid 133770) or His$_6$-SUMO2 (Addgene plasmid 133771) using Mirus TransIT-LT1 transfection reagent. Twenty-four hours after transfection, the transfection mix was removed, and the cells were allowed to recover in fresh media for 48 h before harvest. Purifications of polypeptides conjugated with His$_6$-SUMO1 or His$_6$-SUMO2 were performed by following the protocol described by Tatham et al. (2009) using nickel–nitrilotriacetic acid (Ni-NTA) agarose beads (Qiagen 30230) following the manufacturer's protocol. Briefly, cells were lysed in cell lysis buffer (6 M guanidinium-HCl, 10 mM Tris-HCl, 100 mM sodium phosphate buffer at pH 8.0, 20 mM NEM, 10 mM imidazole [Sigma I2399], 5 mM β-mercaptoethanol [Sigma M3148]). Cell lysates were sonicated for 45 sec and cleared by centrifugation at 3000g for 15 min at room temperature. The supernatants were subjected to purification of His-tagged peptides with prewashed Ni-NTA agarose beads overnight at 4°C. Samples were then washed sequentially with (1) cell lysis buffer supplemented with 0.01% (v/v) Triton X-100, (2) pH 8.0 wash buffer (8 M urea, 10 mM Tris-HCl, 100 mM sodium phosphate buffer at pH 8.0, 20 mM NEM, 10 mM imidazole, 0.1% [v/v] Triton X-100, 5 mM β-mercaptoethanol), and (3) pH 6.3 wash buffer (8 M urea, 10 mM Tris-HCl, 100 mM sodium phosphate buffer at pH 6.30, 20 mM NEM, 10 mM imidazole, 0.1% [v/v] Triton X-100, 5 mM β-mercaptoethanol). Purified samples were eluted in elution buffer (200 mM imidazole, 5% [w/v] sodium dodecyl sulfate, 150 mM Tris-HCl, 30% [v/v] glycerol, 720 mM β-mercaptoethanol, 0.0025% [w/v] bromophenol blue) for 30 min at room temperature.

Purification of SUMO-conjugated peptides

SUMO-conjugated polypeptides in subcellular fractionation samples were purified with biotin SUMO capture reagent (Biotin S-Cap, LifeSensors, Inc. SM-101) following the manufacturer's protocol. Prior to binding of SUMO-conjugated polypeptides, the concentrations of NP-40 in cytoplasmic fractionation samples were adjusted to 0.2% (v/v) NP-40 with dilution buffer (100 mM Tris-HCl at pH 8.0, 150 mM NaCl, 5 mM EDTA at pH 8.0). Samples were incubated with 1 µM biotin S-Cap for 2 h on ice. Following the biotin S-Cap reagent binding reaction, the input control samples were collected, and the remaining samples were incubated with Dynabeads M-280 streptavidin magnetic beads (Invitrogen 11206D) for 2 h at 4°C on an end-over-end rotator. Following the binding reaction of the biotin S-Cap reagent to streptavidin beads, the unbound fractions were collected. The pull-down samples bound to streptavidin beads were washed four times with wash buffer (100 mM Tris-HCl at pH 8.0, 150 mM NaCl, 5 mM EDTA at pH 8.0, 0.05% [v/v] NP-40, 0.1% [v/v] Tween-20, 5 mM NEM, 1× protease inhibitor cocktail [Roche 11836170001]) and eluted by boiling for 5 min at 95°C.

Mass spectrometry

For preparation of purified SUMO-conjugated peptides for mass spectrometry analysis, chromatin extracts were acquired using the subfractionation process described above. Four milligrams of total protein from each sample was subjected to binding of SUMO-conjugated polypeptides to 1 µM biotin S-Cap in a total volume of 200 µL of binding reaction for 2 h on ice. The samples were then incubated with streptavidin Sepharose high-performance agarose beads (Cytiva, GE Healthcare 17-5113-01) overnight at 4°C on an end-over-end rotator. Beads were washed sequentially (1) four times with wash buffer (100 mM Tris-HCl at pH 8.0, 150 mM NaCl, 5 mM EDTA at pH 8.0, 0.05% [v/v] NP-40, 0.1% [v/v] Tween-20, 5 mM NEM, 1× protease inhibitor cocktail), (2) once with TNNE wash buffer (25 mM Tris-HCl at pH 7.40, 150 mM NaCl, 0.1% NP-40, 1 mM EDTA), and (3) three times with ABC buffer (50 mM ammonium bicarbonate at pH 8.0). Tryptic digestion was performed on beads using 1 µg of trypsin (BioShop T6567) dissolved in ABC buffer overnight at 37°C, followed by extended incubation with an additional 0.5 µg of trypsin for 3 h. The digested peptide samples (supernatant) were lyophilized using vacuum centrifugation without heating.

Data-dependent acquisition liquid chromatography with tandem mass spectrometry analysis was performed by the Network Biology Collaborative Centre (NBCC) Proteomics Facility at the Lunenfeld-Tanenbaum Research Institute. The lyophilized digested peptides were loaded onto Evotip Pure (per the manufacturer's instructions) and the performance column (8 cm × 150 µm with 1.5-µm beads; Evosep EV-1109) and then eluted from the column at 40°C using the preformed acetonitrile gradient with the 60 SPD (samples per day) method generated by an Evosep One system. Tandem mass spectrometry analysis was performed with the eluted peptides for 22 min using timsTOF Pro 2 (Bruker) in data-dependent mode. For data extraction from mass spectrometry analysis, MSFragger 3.7 was used within the ProHits LIMS platform. The experimental data were searched against the human reference proteome database from UniProt (UP000005640), and trypsin specificity (two missed cleavages), N-terminal acetylation, and oxidized methionine were set as variable modifications. For data analysis, only proteins with a minimum probability of 0.5 were considered, and redundant peptides were not removed. To assign Q-values and posterior error probabilities (PEPs) for each match, the target–decoy competition method was used. Precursor and fragment mass tolerance was set to 30 ppm. The hit proteins

were identified using an FDR filter set to 0.01, and FDR for each match was estimated by using the razor peptide method and both a filtered peptide-spectrum match (PSM) score and a protein list.

Data sets

The data sets generated and analyzed during this study are available in the following source data files: NCBI BioProject: PRJNA1085024, MassIVE: MSV000094236, and ProteomeXChange: PXD050361.

Competing interest statement

Acknowledgments

References

Adam S, Rossi SE, Moatti N, De Marco Zompit M, Xue Y, Ng TF, Álvarez-Quilón A, Desjardins J, Bhaskaran V, Martino G, et al. 2021. The CIP2A–TOPBP1 axis safeguards chromosome stability and is a synthetic lethal target for BRCA-mutated cancer. *Nat Cancer* **2:** 1357–1371. doi:10.1038/s43018-021-00266-w

Adamus M, Lelkes E, Potesil D, Ganji SR, Kolesar P, Zabrady K, Zdrahal Z, Palecek JJ. 2020. Molecular insights into the architecture of the human SMC5/6 complex. *J Mol Biol* **432:** 3820–3837. doi:10.1016/j.jmb.2020.04.024

Aragón L. 2018. The Smc5/6 complex: new and old functions of the enigmatic long-distance relative. *Annu Rev Genet* **52:** 89–107. doi:10.1146/annurev-genet-120417-031353

Baba D, Maita N, Jee JG, Uchimura Y, Saitoh H, Sugasawa K, Hanaoka F, Tochio H, Hiroaki H, Shirakawa M. 2005. Crystal structure of thymine DNA glycosylase conjugated to SUMO-1. *Nature* **435:** 979–982. doi:10.1038/nature03634

Boddy MN, Shanahan P, McDonald WH, Lopez-Girona A, Noguchi E, Yates IJ, Russell P. 2003. Replication checkpoint kinase Cds1 regulates recombinational repair protein Rad60. *Mol Cell Biol* **23:** 5939–5946. doi:10.1128/MCB.23.16.5939-5946.2003

Branzei D, Sollier J, Liberi G, Zhao X, Maeda D, Seki M, Enomoto T, Ohta K, Foiani M. 2006. Ubc9- and mms21-mediated sumoylation counteracts recombinogenic events at damaged replication forks. *Cell* **127:** 509–522. doi:10.1016/j.cell.2006.08.050

Brinkman EK, Chen T, Amendola M, van Steensel B. 2014. Easy quantitative assessment of genome editing by sequence trace decomposition. *Nucleic Acids Res* **42:** e168. doi:10.1093/nar/gku936

Bryant P, Pozzati G, Elofsson A. 2022. Improved prediction of protein–protein interactions using AlphaFold2. *Nat Commun* **13:** 1265. doi:10.1038/s41467-022-28865-w

Bythell-Douglas R, Deans AJ. 2021. A structural guide to the bloom syndrome complex. *Structure* **29:** 99–113. doi:10.1016/j.str.2020.11.020

Chan YW, West SC. 2014. Spatial control of the GEN1 Holliday junction resolvase ensures genome stability. *Nat Commun* **5:** 4844. doi:10.1038/ncomms5844

Choi K, Szakal B, Chen YH, Branzei D, Zhao X. 2010. The Smc5/6 complex and Esc2 influence multiple replication-associated recombination processes in *Saccharomyces cerevisiae*. *Mol Biol Cell* **21:** 2306–2314. doi:10.1091/mbc.e10-01-0050

Colic M, Wang G, Zimmermann M, Mascall K, McLaughlin M, Bertolet L, Lenoir WF, Moffat J, Angers S, Durocher D, et al. 2019. Identifying chemogenetic interactions from CRISPR screens with DrugZ. *Genome Med* **11:** 52. doi:10.1186/s13073-019-0665-3

De Marco Zompit M, Esteban MT, Mooser C, Adam S, Rossi SE, Jeanrenaud A, Leimbacher PA, Fink D, Shorrocks AK, Blackford AN, et al. 2022. The CIP2A–TOPBP1 complex safeguards chromosomal stability during mitosis. *Nat Commun* **13:** 4143. doi:10.1038/s41467-022-31865-5

Dempster JM, Rossen J, Kazachkova M, Pan J, Kugener G, Root DE, Tsherniak A. 2019. Extracting biological insights from the Project Achilles genome-scale CRISPR screens in cancer cell lines. bioRxiv doi:10.1101/720243

Evans R, O'Neill M, Pritzel A, Antropova N, Senior A, Green T, Žídek A, Bates R, Blackwell S, Yim J, et al. 2021. Protein complex prediction with AlphaFold-Multimer. bioRxiv doi:10.1101/2021.10.04.463034

Fenech M, Kirsch-Volders M, Natarajan AT, Surralles J, Crott JW, Parry J, Norppa H, Eastmond DA, Tucker JD, Thomas P. 2011. Molecular mechanisms of micronucleus, nucleoplasmic bridge and nuclear bud formation in mammalian and human cells. *Mutagenesis* **26:** 125–132. doi:10.1093/mutage/geq052

Fradet-Turcotte A, Canny MD, Escribano-Díaz C, Orthwein A, Leung CC, Huang H, Landry MC, Kitevski-Leblanc J, Noordermeer SM, Sicheri F, et al. 2013. 53BP1 is a reader of the DNA-damage-induced H2A Lys 15 ubiquitin mark. *Nature* **499:** 50–54. doi:10.1038/nature12318

Fraschilla I, Jeffrey KL. 2020. The speckled protein (SP) family: immunity's chromatin readers. *Trends Immunol* **41:** 572–585. doi:10.1016/j.it.2020.04.007

Galanty Y, Belotserkovskaya R, Coates J, Polo S, Miller KM, Jackson SP. 2009. Mammalian SUMO E3-ligases PIAS1 and PIAS4 promote responses to DNA double-strand breaks. *Nature* **462:** 935–939. doi:10.1038/nature08657

Gallego-Paez LM, Tanaka H, Bando M, Takahashi M, Nozaki N, Nakato R, Shirahige K, Hirota T. 2014. Smc5/6-mediated regulation of replication progression contributes to chromosome

assembly during mitosis in human cells. *Mol Biol Cell* **25:** 302–317. doi:10.1091/mbc.e13-01-0020

Gallo D, Young JTF, Fourtounis J, Martino G, Álvarez-Quilón A, Bernier C, Duffy NM, Papp R, Roulston A, Stocco R, et al. 2022. CCNE1 amplification is synthetic lethal with PKMYT1 kinase inhibition. *Nature* **604:** 749–756. doi:10.1038/s41586-022-04638-9

Ge SX, Jung D, Yao R. 2020. ShinyGO: a graphical gene-set enrichment tool for animals and plants. *Bioinformatics* **36:** 2628–2629. doi:10.1093/bioinformatics/btz931

Goddard TD, Huang CC, Meng EC, Pettersen EF, Couch GS, Morris JH, Ferrin TE. 2018. UCSF chimerax: meeting modern challenges in visualization and analysis. *Protein Sci* **27:** 14–25. doi:10.1002/pro.3235

Hardeland U, Steinacher R, Jiricny J, Schär P. 2002. Modification of the human thymine-DNA glycosylase by ubiquitin-like proteins facilitates enzymatic turnover. *EMBO J* **21:** 1456–1464. doi:10.1093/emboj/21.6.1456

Hart T, Chandrashekhar M, Aregger M, Steinhart Z, Brown KR, MacLeod G, Mis M, Zimmermann M, Fradet-Turcotte A, Sun S, et al. 2015. High-resolution CRISPR screens reveal fitness genes and genotype-specific cancer liabilities. *Cell* **163:** 1515–1526. doi:10.1016/j.cell.2015.11.015

Hart T, Tong AHY, Chan K, Van Leeuwen J, Seetharaman A, Aregger M, Chandrashekhar M, Hustedt N, Seth S, Noonan A, et al. 2017. Evaluation and design of genome-wide CRISPR/SpCas9 knockout screens. *G3* **7:** 2719–2727. doi:10.1534/g3.117.041277

Heideker J, Prudden J, Perry JJ, Tainer JA, Boddy MN. 2011. SUMO-targeted ubiquitin ligase, Rad60, and Nse2 SUMO ligase suppress spontaneous Top1-mediated DNA damage and genome instability. *PLoS Genet* **7:** e1001320. doi:10.1371/journal.pgen.1001320

Hendriks IA, Vertegaal AC. 2016. A comprehensive compilation of SUMO proteomics. *Nat Rev Mol Cell Biol* **17:** 581–595. doi:10.1038/nrm.2016.81

Hertz EPT, Vega IA, Kruse T, Wang Y, Hendriks IA, Bizard AH, Eugui-Anta A, Hay RT, Nielsen ML, Nilsson J, et al. 2023. The SUMO–NIP45 pathway processes toxic DNA catenanes to prevent mitotic failure. *Nat Struct Mol Biol* **30:** 1303–1313. doi:10.1038/s41594-023-01045-0

Hodge MR, Chun HJ, Rengarajan J, Alt A, Lieberson R, Glimcher LH. 1996. NF-AT-Driven interleukin-4 transcription potentiated by NIP45. *Science* **274:** 1903–1905. doi:10.1126/science.274.5294.1903

Hong Y, Zhang H, Gartner A. 2021. The last chance saloon. *Front Cell Dev Biol* **9:** 671297. doi:10.3389/fcell.2021.671297

Jackson SP, Durocher D. 2013. Regulation of DNA damage responses by ubiquitin and SUMO. *Mol Cell* **49:** 795–807. doi:10.1016/j.molcel.2013.01.017

Jacome A, Gutierrez-Martinez P, Schiavoni F, Tenaglia E, Martinez P, Rodríguez-Acebes S, Lecona E, Murga M, Mendez J, Blasco MA, et al. 2015. NSMCE2 suppresses cancer and aging in mice independently of its SUMO ligase activity. *EMBO J* **34:** 2604–2619. doi:10.15252/embj.201591829

Jumper J, Evans R, Pritzel A, Green T, Figurnov M, Ronneberger O, Tunyasuvunakool K, Bates R, Žídek A, Potapenko A, et al. 2021. Highly accurate protein structure prediction with AlphaFold. *Nature* **596:** 583–589. doi:10.1038/s41586-021-03819-2

Kim E, Hart T. 2021. Improved analysis of CRISPR fitness screens and reduced off-target effects with the BAGEL2 gene essentiality classifier. *Genome Med* **13:** 2. doi:10.1186/s13073-020-00809-3

Langston SP, Grossman S, England D, Afroze R, Bence N, Bowman D, Bump N, Chau R, Chuang BC, Claiborne C, et al. 2021. Discovery of TAK-981, a first-in-class inhibitor of SUMO-activating enzyme for the treatment of cancer. *J Med Chem* **64:** 2501–2520. doi:10.1021/acs.jmedchem.0c01491

Lightcap ES, Yu P, Grossman S, Song K, Khattar M, Xega K, He X, Gavin JM, Imaichi H, Garnsey JJ, et al. 2021. A small-molecule SUMOylation inhibitor activates antitumor immune responses and potentiates immune therapies in preclinical models. *Sci Transl Med* **13:** eaba7791. doi:10.1126/scitranslmed.aba7791

Matunis MJ, Coutavas E, Blobel G. 1996. A novel ubiquitin-like modification modulates the partitioning of the Ran-GTPase-activating protein RanGAP1 between the cytosol and the nuclear pore complex. *J Cell Biol* **135:** 1457–1470. doi:10.1083/jcb.135.6.1457

Mirdita M, Schütze K, Moriwaki Y, Heo L, Ovchinnikov S, Steinegger M. 2022. ColabFold: making protein folding accessible to all. *Nat Methods* **19:** 679–682. doi:10.1038/s41592-022-01488-1

Miyabe I, Morishita T, Hishida T, Yonei S, Shinagawa H. 2006. Rhp51-dependent recombination intermediates that do not generate checkpoint signal are accumulated in *Schizosaccharomyces pombe* rad60 and smc5/6 mutants after release from replication arrest. *Mol Cell Biol* **26:** 343–353. doi:10.1128/MCB.26.1.343-353.2006

Morishita T, Tsutsui Y, Iwasaki H, Shinagawa H. 2002. The *Schizosaccharomyces pombe* rad60 gene is essential for repairing double-strand DNA breaks spontaneously occurring during replication and induced by DNA-damaging agents. *Mol Cell Biol* **22:** 3537–3548. doi:10.1128/MCB.22.10.3537-3548.2002

Morris JR, Boutell C, Keppler M, Densham R, Weekes D, Alamshah A, Butler L, Galanty Y, Pangon L, Kiuchi T, et al. 2009. The SUMO modification pathway is involved in the BRCA1 response to genotoxic stress. *Nature* **462:** 886–890. doi:10.1038/nature08593

Nacerddine K, Lehembre F, Bhaumik M, Artus J, Cohen-Tannoudji M, Babinet C, Pandolfi PP, Dejean A. 2005. The SUMO pathway is essential for nuclear integrity and chromosome segregation in mice. *Dev Cell* **9:** 769–779. doi:10.1016/j.devcel.2005.10.007

Noordermeer SM, Adam S, Setiaputra D, Barazas M, Pettitt SJ, Ling AK, Olivieri M, Álvarez-Quilón A, Moatti N, Zimmermann M, et al. 2018. The shieldin complex mediates 53BP1-dependent DNA repair. *Nature* **560:** 117–121. doi:10.1038/s41586-018-0340-7

Novatchkova M, Bachmair A, Eisenhaber B, Eisenhaber F. 2005. Proteins with two SUMO-like domains in chromatin-associated complexes: the RENi (Rad60–Esc2–NIP45) family. *BMC Bioinformatics* **6:** 22. doi:10.1186/1471-2105-6-22

Olivieri M, Durocher D. 2021. Genome-scale chemogenomic CRISPR screens in human cells using the TKOv3 library. *STAR Protoc* **2:** 100321. doi:10.1016/j.xpro.2021.100321

Olivieri M, Cho T, Álvarez-Quilón A, Li K, Schellenberg MJ, Zimmermann M, Hustedt N, Rossi SE, Adam S, Melo H, et al. 2020. A genetic map of the response to DNA damage in human cells. *Cell* **182:** 481–496.e21. doi:10.1016/j.cell.2020.05.040

Payne F, Colnaghi R, Rocha N, Seth A, Harris J, Carpenter G, Bottomley WE, Wheeler E, Wong S, Saudek V, et al. 2014. Hypomorphism in human NSMCE2 linked to primordial dwarfism and insulin resistance. *J Clin Invest* **124:** 4028–4038. doi:10.1172/JCI73264

Peng XP, Zhao X. 2023. The multi-functional Smc5/6 complex in genome protection and disease. *Nat Struct Mol Biol* **30:** 724–734. doi:10.1038/s41594-023-01015-6

Potts PR, Yu H. 2005. Human MMS21/NSE2 is a SUMO ligase required for DNA repair. *Mol Cell Biol* **25:** 7021–7032. doi:10.1128/MCB.25.16.7021-7032.2005

Prudden J, Pebernard S, Raffa G, Slavin DA, Perry JJ, Tainer JA, McGowan CH, Boddy MN. 2007. SUMO-targeted ubiquitin ligases in genome stability. *EMBO J* **26:** 4089–4101. doi:10.1038/sj.emboj.7601838

Prudden J, Perry JJ, Arvai AS, Tainer JA, Boddy MN. 2009. Molecular mimicry of SUMO promotes DNA repair. *Nat Struct Mol Biol* **16:** 509–516. doi:10.1038/nsmb.1582

Prudden J, Perry JJ, Nie M, Vashisht AA, Arvai AS, Hitomi C, Guenther G, Wohlschlegel JA, Tainer JA, Boddy MN. 2011. DNA repair and global sumoylation are regulated by distinct Ubc9 noncovalent complexes. *Mol Cell Biol* **31:** 2299–2310. doi:10.1128/MCB.05188-11

Pryzhkova MV, Jordan PW. 2016. Conditional mutation of Smc5 in mouse embryonic stem cells perturbs condensin localization and mitotic progression. *J Cell Sci* **129:** 1619–1634. doi:10.1242/jcs.179036

Psakhye I, Jentsch S. 2012. Protein group modification and synergy in the SUMO pathway as exemplified in DNA repair. *Cell* **151:** 807–820. doi:10.1016/j.cell.2012.10.021

Räschle M, Smeenk G, Hansen RK, Temu T, Oka Y, Hein MY, Nagaraj N, Long DT, Walter JC, Hofmann K, et al. 2015. Proteomics reveals dynamic assembly of repair complexes during bypass of DNA cross-links. *Science* **348:** 1253671. doi:10.1126/science.1253671

Robey RW, Pluchino KM, Hall MD, Fojo AT, Bates SE, Gottesman MM. 2018. Revisiting the role of ABC transporters in multidrug-resistant cancer. *Nat Rev Cancer* **18:** 452–464. doi:10.1038/s41568-018-0005-8

Roy S, Schlacher K. 2019. SIRF: a single-cell assay for in situ protein interaction with nascent DNA replication forks. *Bio Protoc* **9:** e3377. doi:10.21769/BioProtoc.3377

Roy S, Luzwick JW, Schlacher K. 2018. SIRF: quantitative in situ analysis of protein interactions at DNA replication forks. *J Cell Biol* **217:** 1521–1536. doi:10.1083/jcb.201709121

Sanjana NE, Shalem O, Zhang F. 2014. Improved vectors and genome-wide libraries for CRISPR screening. *Nat Methods* **11:** 783–784. doi:10.1038/nmeth.3047

Sebesta M, Urulangodi M, Stefanovie B, Szakal B, Pacesa M, Lisby M, Branzei D, Krejci L. 2017. Esc2 promotes Mus81 complex-activity via its SUMO-like and DNA binding domains. *Nucleic Acids Res* **45:** 215–230. doi:10.1093/nar/gkw882

Sekiyama N, Arita K, Ikeda Y, Hashiguchi K, Ariyoshi M, Tochio H, Saitoh H, Shirakawa M. 2010. Structural basis for regulation of poly-SUMO chain by a SUMO-like domain of Nip45. *Proteins* **78:** 1491–1502. doi:10.1002/prot.22667

Sifri C, Hoeg L, Durocher D, Setiaputra D. 2023. An AlphaFold2 map of the 53BP1 pathway identifies a direct SHLD3–RIF1 interaction critical for shieldin activity. *EMBO Rep* **24:** e56834. doi:10.15252/embr.202356834

Sollier J, Driscoll R, Castellucci F, Foiani M, Jackson SP, Branzei D. 2009. The *Saccharomyces cerevisiae* Esc2 and Smc5-6 proteins promote sister chromatid junction-mediated intra-S repair. *Mol Biol Cell* **20:** 1671–1682. doi:10.1091/mbc.e08-08-0875

Soucy TA, Smith PG, Milhollen MA, Berger AJ, Gavin JM, Adhikari S, Brownell JE, Burke KE, Cardin DP, Critchley S, et al. 2009. An inhibitor of NEDD8-activating enzyme as a new approach to treat cancer. *Nature* **458:** 732–736. doi:10.1038/nature07884

Stirling DR, Swain-Bowden MJ, Lucas AM, Carpenter AE, Cimini BA, Goodman A. 2021. Cellprofiler 4: improvements in speed, utility and usability. *BMC Bioinformatics* **22:** 433. doi:10.1186/s12859-021-04344-9

Szklarczyk D, Gable AL, Nastou KC, Lyon D, Kirsch R, Pyysalo S, Doncheva NT, Legeay M, Fang T, Bork P, et al. 2021. The STRING database in 2021: customizable protein-protein networks, and functional characterization of user-uploaded gene/measurement sets. *Nucleic Acids Res* **49:** D605–D612. doi:10.1093/nar/gkaa1074

Taipale M, Tucker G, Peng J, Krykbaeva I, Lin ZY, Larsen B, Choi H, Berger B, Gingras AC, Lindquist S. 2014. A quantitative chaperone interaction network reveals the architecture of cellular protein homeostasis pathways. *Cell* **158:** 434–448. doi:10.1016/j.cell.2014.05.039

Tatham MH, Rodriguez MS, Xirodimas DP, Hay RT. 2009. Detection of protein SUMOylation in vivo. *Nat Protoc* **4:** 1363–1371. doi:10.1038/nprot.2009.128

Ulrich HD, Vogel S, Davies AA. 2005. SUMO keeps a check on recombination during DNA replication. *Cell Cycle* **4:** 1699–1702. doi:10.4161/cc.4.12.2194

Urulangodi M, Sebesta M, Menolfi D, Szakal B, Sollier J, Sisakova A, Krejci L, Branzei D. 2015. Local regulation of the Srs2 helicase by the SUMO-like domain protein Esc2 promotes recombination at sites of stalled replication. *Genes Dev* **29:** 2067–2080. doi:10.1101/gad.265629.115

Varejão N, Lascorz J, Codina-Fabra J, Bellí G, Borràs-Gas H, Torres-Rosell J, Reverter D. 2021. Structural basis for the E3 ligase activity enhancement of yeast Nse2 by SUMO-interacting motifs. *Nat Commun* **12:** 7013. doi:10.1038/s41467-021-27301-9

Venegas AB, Natsume T, Kanemaki M, Hickson ID. 2020. Inducible degradation of the human SMC5/6 complex reveals an essential role only during interphase. *Cell Rep* **31:** 107533. doi:10.1016/j.celrep.2020.107533

Vertegaal ACO. 2022. Signalling mechanisms and cellular functions of SUMO. *Nat Rev Mol Cell Biol* **23:** 715–731. doi:10.1038/s41580-022-00500-y

Vondrova L, Kolesar P, Adamus M, Nociar M, Oliver AW, Palecek JJ. 2020. A role of the Nse4 kleisin and Nse1/Nse3 KITE subunits in the ATPase cycle of SMC5/6. *Sci Rep* **10:** 9694. doi:10.1038/s41598-020-66647-w

Warecki B, Sullivan W. 2020. Mechanisms driving acentric chromosome transmission. *Chromosome Res* **28:** 229–246. doi:10.1007/s10577-020-09636-z

Wessel SR, Mohni KN, Luzwick JW, Dungrawala H, Cortez D. 2019. Functional analysis of the replication fork proteome identifies BET proteins as PCNA regulators. *Cell Rep* **28:** 3497–3509.e4. doi:10.1016/j.celrep.2019.08.051

Xu Y, Plechanovová A, Simpson P, Marchant J, Leidecker O, Kraatz S, Hay RT, Matthews SJ. 2014. Structural insight into SUMO chain recognition and manipulation by the ubiquitin ligase RNF4. *Nat Commun* **5:** 4217. doi:10.1038/ncomms5217

Yu Y, Li S, Ser Z, Sanyal T, Choi K, Wan B, Kuang H, Sali A, Kentsis A, Patel DJ, et al. 2021. Integrative analysis reveals unique structural and functional features of the Smc5/6 complex. *Proc Natl Acad Sci* **118:** e2026844118. doi:10.1073/pnas.2026844118

Yu Y, Li S, Ser Z, Kuang H, Than T, Guan D, Zhao X, Patel DJ. 2022. Cryo-EM structure of DNA-bound Smc5/6 reveals DNA clamping enabled by multi-subunit conformational changes. *Proc Natl Acad Sci* **119:** e2202799119. doi:10.1073/pnas.2202799119

Zimmermann M, Murina O, Reijns MAM, Agathanggelou A, Challis R, Tarnauskaite Z, Muir M, Fluteau A, Aregger M, McEwan A, et al. 2018. CRISPR screens identify genomic ribonucleotides as a source of PARP-trapping lesions. *Nature* **559:** 285–289. doi:10.1038/s41586-018-0291-z